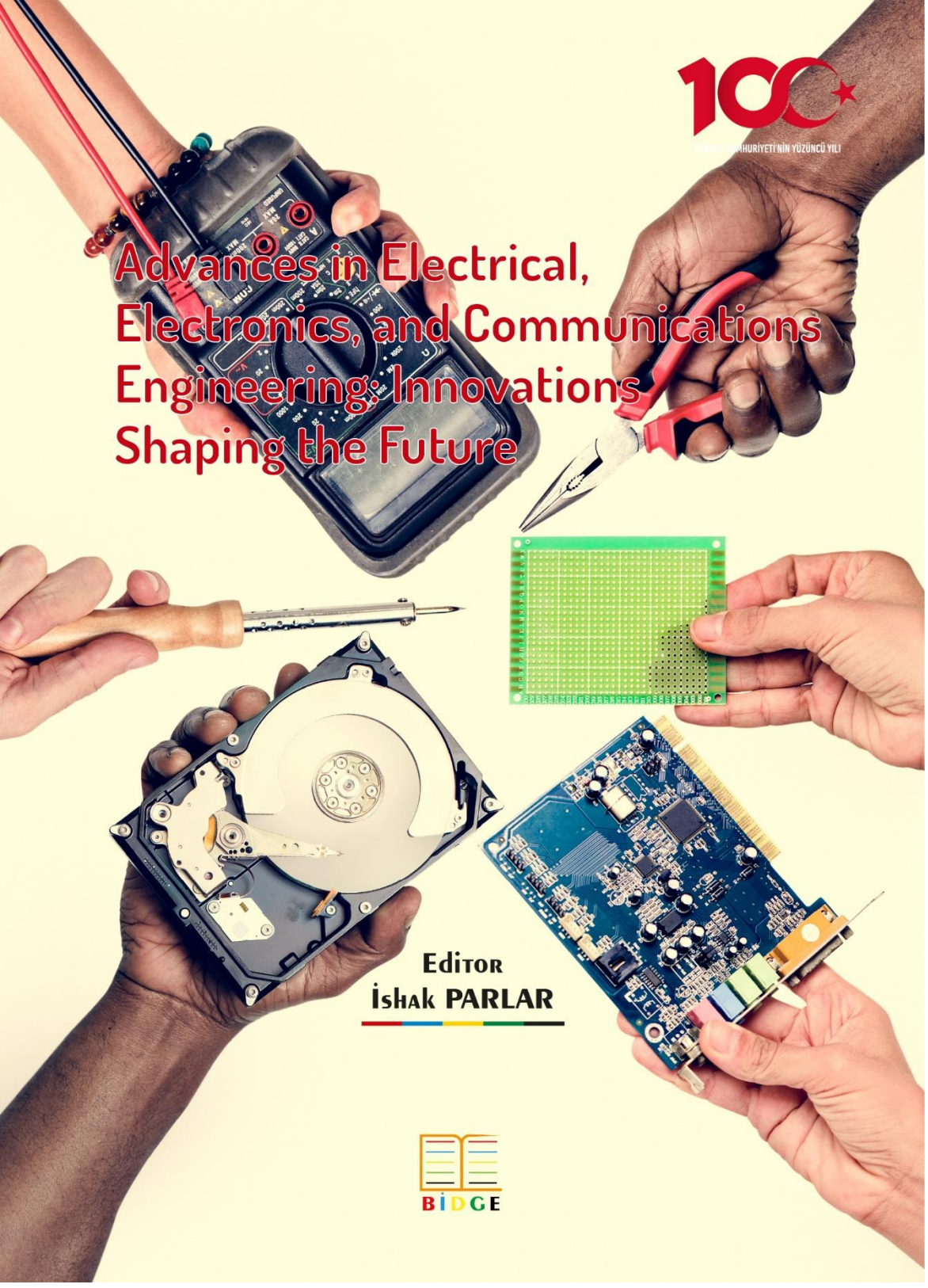

Advances in Electrical, Electronics, and Communications Engineering: Innovations Shaping the Future

Editor
İshak PARLAR

BİDGE

BIDGE Publications

Advances in Electrical, Electronics, and Communications Engineering: Innovations Shaping the Future

Editor: Asst. Prof. İshak PARLAR

ISBN: 978-625-372-198-5

Page Layout: Gözde YÜCEL

1st Edition:

Publication Date: 25.06.2024

BIDGE Publications,

Certificate No: 71374

www.bidgeyayinlari.com.tr - bidgeyayinlari@gmail.com

Krc Bilişim Ticaret ve Organizasyon Ltd. Şti.
Güzeltepe Mahallesi Abidin Daver Sokak Sefer Apartmanı No: 7/9 Çankaya / Ankara

PREFACE

Innovation in the rapidly developing field of electrical, electronics and communications engineering continues to be the driving force that pushes boundaries and transforms theoretical concepts into practical applications. This book represents a compendium of cutting-edge research and technological advances in various specialties in this broad field.

Initial work begins with the intricacies of high-Q factor dual resonance visible plasmonic arrays. Additionally, the design considerations taken into account in the development of low voltage harness for L6-L7 vehicles are discussed in detail. It then continues into the field of metamaterials, focusing on titanium nitride-based metasurfaces designed to achieve precise light deflection at 1550 nm. Finally, it is shown that the integration of deep learning-based frameworks for colon cancer detection from histopathological images can lead to earlier detection and better patient outcomes for the use of artificial intelligence in medical diagnoses.

This foreword aims to summarize the scope and importance of the topics covered in your book, highlighting their relevance, innovativeness, and potential impact on various sectors of engineering and beyond.

Editor

Asst. Prof. İshak PARLAR

Content

CHAPTER I

High Q-Factor Dual Resonance Visible Plasmonic Array

Hayriye DEMİRTAS[1]
Mustafa TURKMEN[2]
Ekin ASLAN[3]
Erdem ASLAN[4]

Introduction

Aperture-based plasmonic nanoantennas have emerged as a significant field of study due to their ability to focus and manipulate light at the nanoscale, providing numerous technological applications (Maier, 2007). These nanoantennas consist of sub-wavelength apertures, such as slits or holes, in metal

[1] Ph.D. Candidate, Erciyes University, Department of Electrical and Electronics Engineering, Orcid: 0000-0002-1015-0235
[2] Prof. Dr., Erciyes University, Department of Electrical and Electronics Engineering, Orcid: 0000-0002-5257-8256
[3] Assoc. Prof, Kayseri University, Department of Electrical and Electronics Engineering, Orcid: 0000-0003-0933-7796
[4] Assoc. Prof, Erciyes University, Department of Electrical and Electronics Engineering, Orcid: 0000-0001-6829-9000

films that enable the excitation of surface plasmons (Barnes et al., 2003). At the metal-dielectric interface, surface plasmons manifest as collective oscillations of free electrons, capable of interacting with incident light to yield remarkable optical properties (Ozbay, 2006).

The fundamental working principle of aperture-based plasmonic nanoantennas revolves around the excitation of localized surface plasmon resonances (LSPRs) within the apertures (Schuller et al., 2010). These resonances lead to significant enhancements in the local electromagnetic fields, which can be tailored by adjusting the geometry and arrangement of the apertures (Johnson & Christy, 1972). Metals like gold (Au) and silver (Ag) are often employed due to their favorable plasmonic characteristics in the visible and near-infrared spectral regions (Anker et al., 2009).

The size, shape, and arrangement of apertures critically effect the performance of nanoantennas. For example, circular, rectangular, and bowtie-shaped apertures have been extensively studied, each offering unique advantages in field enhancement and spectral response (Novotny & Hecht, 2006). Additionally, the periodic arrangement of apertures can lead to the formation of photonic band gaps and enhanced transmission spectra, further broadening the functional capabilities of these nanoantennas (Knight et al., 2011). Finite-Difference Time-Domain (FDTD) simulations are commonly used to design and optimize aperture-based plasmonic nanoantennas. These simulations provide detailed insights into the electromagnetic field distributions, resonance modes, and transmission/reflection properties of the nanoantennas (Taflove et al., 2005). By leveraging these computational tools,

researchers can precisely control the design parameters to achieve desired optical responses (Lal et al., 2007).

Aperture-based plasmonic nanoantennas are used applications in various fields. In biosensing applications, the enhanced local fields around the apertures are used to detect biomolecules with high sensitivity. The shift in resonance frequency upon binding of the target molecule to the nanoantenna surface allows for label-free detection (Nie & Emory, 1997). In a similar vein, these nanoantennas are employed in surface-enhanced Raman scattering (SERS), leveraging the localized field enhancement to markedly augment the Raman signal emanating from molecules attached to the metal surface (Stewart et al., 2008). In the realm of photonics, aperture-based nanoantennas are integrated into optical circuits to manipulate light at sub-wavelength scales, enabling compact and efficient photonic devices. They play a crucial role in enhancing light-matter interactions, crucial for applications such as nonlinear optics and quantum information processing (Mayer & Hafner, 2011). Moreover, the ability of these nanoantennas to concentrate light into nanoscopic volumes makes them ideal for high-resolution imaging and spectroscopy (Zia et al., 2006). Environmental sensing is another area where these nanoantennas are highly effective. They can detect trace amounts of pollutants or hazardous chemicals by monitoring changes in their plasmonic resonance properties, providing real-time and on-site analytical capabilities (Homola, 2008). Immobilization of antibodies and samples to energy-intensive regions of the antenna ensures maximum detection (Cetin et al., 2012), (Cetin, Kaya, et al., 2015), (Cetin, Turkmen, et al., 2015).

Additionally, their small size and compatibility with various substrates make them suitable for integration into portable and wearable devices (Xu et al., 1999). Overall, aperture-based plasmonic nanoantennas represent a versatile and powerful platform for advancing nanophotonics and sensing technologies. Continued research and development in this field promise to unlock new capabilities and applications, driving innovations in various scientific and industrial domains (López-Tejeira et al., 2007).

In this work, we propose aperture based plasmonic nanonantenna design with high Q-factor dual-resonant behavior in the visible (VIS) region. Proposed structure is designed by using double gold (Au) layer with nanoapertures and different spacer dielectric layers such as silicon nitride (Si_3N_4), magnesium fluoride (MgF_2). The resonance response of each nanoantenna varies according to the materials used in its design, the geometric shape and dimensions of the structure, (Cetin et al., 2012), (Cetin, et al., 2015a),(Soler et al., 2017), (Coskun et al., 2014). Additionally, the electric field and magnetic field density regions on the nanoantenna are taken into account in order to make sensitive and accurate sensing with plasmonic nanoantennas.

Method

The nanoantenna design is presented in this study consists of four-arrows facing each other. This nanoantenna with four-arrow shaped nano-aperture is designed and numerically analyzed by using FDTD method. The reflectance, transmittance and electric field distribution analyzes of the structure are also investigated. Transmittance shifts are shown according to the thickness changes of the materials used in the design. The nanoantenna is formed

from down-to-top by a 100 nm thick Si_3N_4 membrane, a 5 nm Au conductor layer, a 100 nm thick MgF_2 layer as the separator and a 5 nm Au top conductor layer. Finally, nano-aperture is etched up to the lowest point in the antenna as shown in Figure 1. In numerical analysis for more sensitive and high accuracy, mesh values are taken small. The nanoantenna's spectral response is investigated by changing dimensions of *a (distance of arrowheads from center), b (width of arrowheads), d (width of arrow), and R (length of arrow).* Moreover transmittance effect of changing thickness of MgF_2 and gold layers are also analyzed. As a novelty, high Q-factor is achieved in this nanoantenna design because of using ultra-thin gold layers.

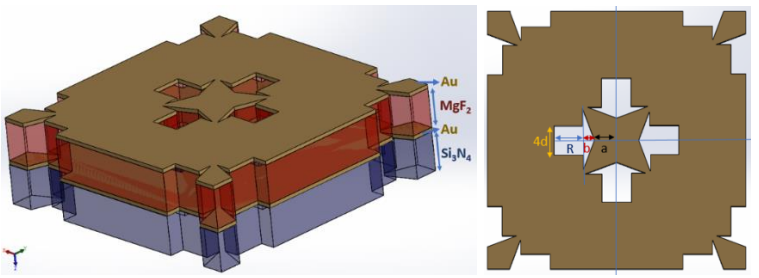

Figure 1. *Design and geometric parameters of aperture-based, four-arrow-shaped nanoantenna construction with double Au conductive layer.*

The alteration in transmittance response is investigated by incrementally varying the 'a' value, representing the distance of arrowheads from the center of the designed nanoantenna (Figure 2.a). The analyses for 'b' values is shown in Figure 2.b., which is the width of arrowheads. Likewise, effect of changing the 'd' value, which is the width of arrow is shown (Figure 2.b). In addition the shift of transmittance response investigated according to the increase 'R' value, which is the length of arrow (Figure 2.c).

Furthermore the transmittance curve is analyzed to assess the impact of increasing the thickness of the MgF_2 layer and its effect on the transmittance curve is analyzed (Figure 3.a). Lastly and most importantly, the effect of the thickness minimization of the gold layers on the spectral response is presented (Figure 3.b). Hence, an in-depth evaluation is carried out to analyze the behavior of the nanoantenna specifically within the visible (VIS) region.

Results

Transmittance responses of the four-arrow-shaped nanoantenna depending on size changes are shown in this work. Figure 2.a shows that the transmittance response has the highest and narrowest peak for a = 60 nm. Likewise, Figure 2.b illustrates that the maximum dual resonance peak value is attained at b = 30 nm. As for the 'd' value, it is found that the change did not have a significant effect on one resonant band. Therefore, d = 20 nm is chosen (Figure 2.c). On the other hand, it is seen that the best peak value among R changes is for R = 80 nm (Figure 2.d).

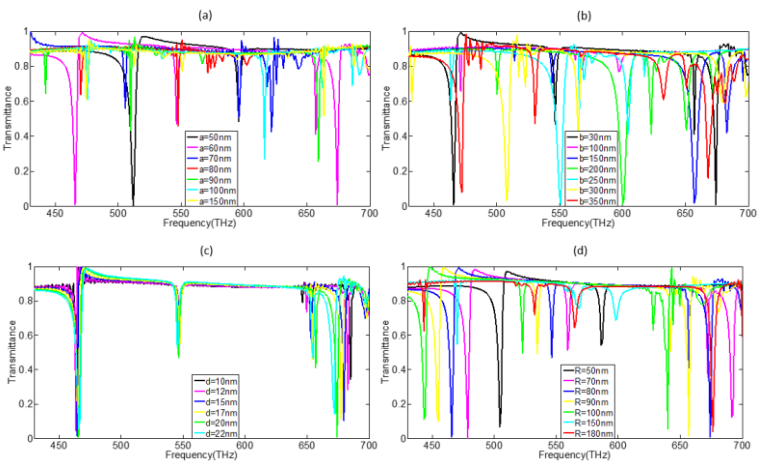

Figure 2. *The influence of dimensional modifications on transmittance response:* ***(a)*** *Alterations in the positioning of arrowheads relative to the center 'a',* ***(b)*** *width of arrowheads 'b',* ***(c)*** *width of arrow 'd' and* ***(d)*** *length of arrow 'R' change of four-arrow-shaped nanoaperture.*

Furthermore, the transmittance response is shown according to dielectric and conductive layer thicknesses in Figure 3.a and Figure 3.b. According to these analyses, it is seen that the resonance has the highest peak value when the MgF_2 thickness is 100 nm thick. On the other hand, it is shown that the resonance response is significantly strengthened for gold layer thickness of 5 nm. Consequently, the analysis reveals that the transmittance response attains its maximum peak value for both resonant bands in the dimensions a = 60 nm, b = 30 nm, d = 20 nm, and R = 80 nm. The optimum values of the dielectric and conductor layer thicknesses are also t_{MgF_2} = 100 nm and t_{Au} = 5 nm.

According to these optimum results, the proposed nanoantenna design is re-analyzed and the best result is shown in Figure 3.c. Consequently, dual resonances with high Q-factor are obtained by using optimum values. The results of the transmittance response are shown dual resonance at 444 nm and 643 nm wavelengths, which are very close to violet (λ = 400 nm - 450 nm) and red (λ = 635 nm – 700 nm), respectively. In proximity to the frequency range, covering biological molecules, the resonance values have reached their peak within a specific region. For this purpose, e-field analyzes are performed and hot points are determined.

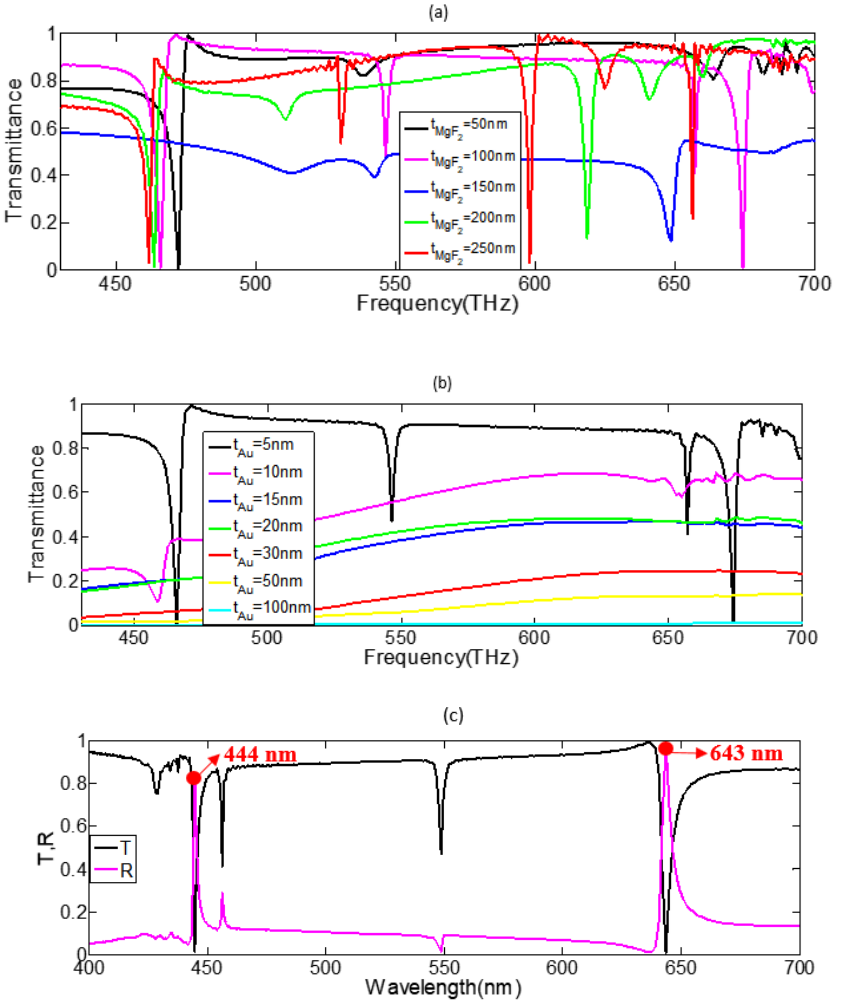

Figure 3. (a) *The alterations in transmittance response corresponds to adjustments in the thickness of the MgF_2 layer and* ***(b)*** *in the thicknesses of Au layers.* ***(c)*** *Transmittance and reflectance curves for optimum dimensions of* $a = 60$ *nm,* $b = 30$ *nm,* $d = 20$ *nm,* $R = 80$ *nm,* $t_{MgF_2} = 100$ *nm, and* $t_{Au} = 5$ *nm.*

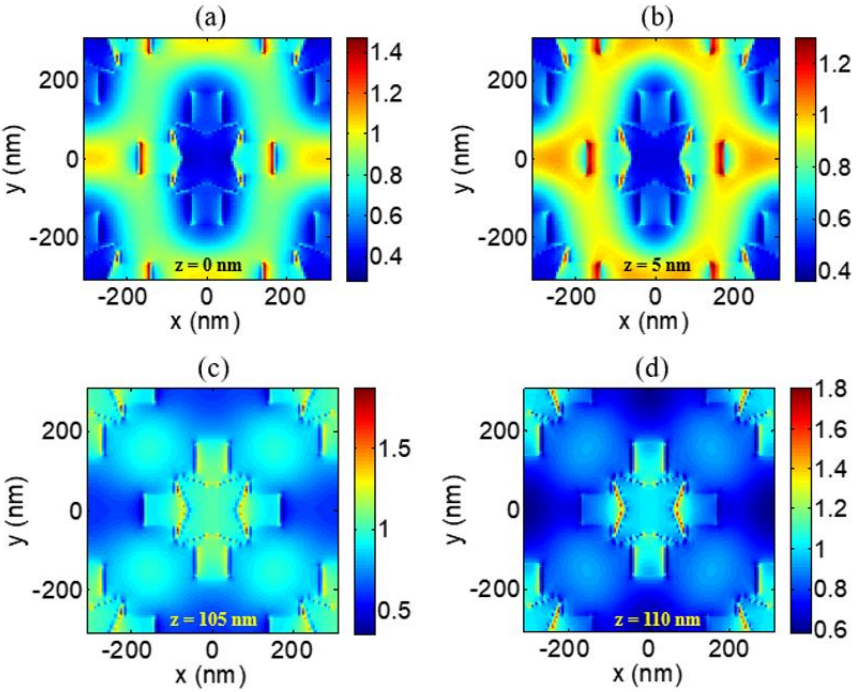

Figure 4. ***(a)*** *Si_3N_4 - Au interlayer field monitor graph (z = 0 nm),* ***(b)*** *Au - MgF_2 first interlayer field monitor graph (z = 5 nm),* ***(c)*** *MgF_2 - Au second interlayer field monitor graph (z = 105 nm), and* ***(d)*** *Au - air second interlayer field monitor graph (z = 110 nm) at λ = 444 nm wavelength.*

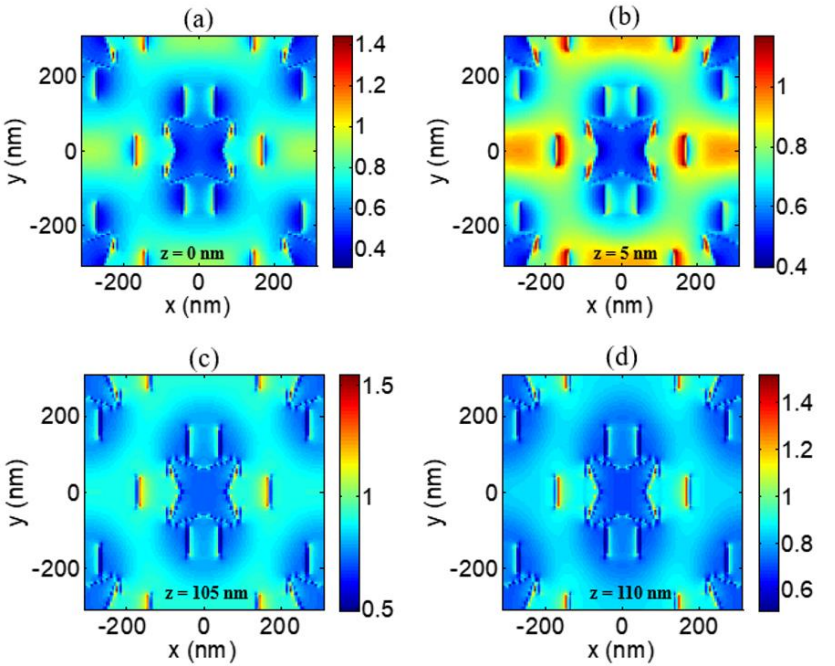

Figure 5. (a) *Si_3N_4 - Au interlayer field monitor graph (z = 0 nm),* ***(b)*** *Au - MgF_2 first interlayer field monitor graph (z = 5 nm),* ***(c)*** *MgF_2 - Au second interlayer field monitor graph (z = 105 nm), and* ***(d)*** *Au - air second interlayer field monitor graph (z = 110 nm) at λ = 643 nm wavelength.*

Electric field intensity distributions are analyzed separately for 444 nm and 643 nm. Since there are double gold layers, four monitors are used, one above and one below each gold surface. Figure 4 shows the electric field intensity distributions of these interlayer monitors for λ = 444 nm respectively. The one for λ = 643 nm is shown in figure 5. The enhancement of molecular vibrational modes in spectroscopic sensing applications is largely determined by the near-field intensity present at the hot-spot locations. (Aslan et al., 2017). Therefore, hot spots in the electric field intensity distribution are very important for biological sensing

applications. Since the characteristic resonances of biological molecules are located in the VIS region, this design with a high Q - factor resonance that can perform in this region offers advantages.

Discussions and Conclusion

Consequently, numerical analysis of a nanoantenna array with high Q-factor dual resonance in the VIS region, obtained by the FDTD method is proposed. As a result of the size and thickness analyses of the antenna, optimum values are determined for dielectric and plasmonic layers. To the best of our knowledge, the investigation of such a small Au layer thickness has not been previously reported in the literature. Using these parameters, the transmittance, the reflectance and electric field intensity analyses of the resized four arrow-shaped nanoantenna design is performed. Finally, dual resonances with a high Q-factor, strong peak- and narrow bands are obtained. These wavelengths are very close to violet and red wavelengths. It is shown that this study will contribute to biological molecule detection applications in the VIS region, thanks to the electric field distributions of the antenna, which have high energy density at strong dual resonances.

Acknowledgement

Hayriye Demirtaş acknowledge the scholarship grant supported by The Council of Higher Education of Turkey (Program Code: YOK 100/2000 PhD Scholarship).

References

Anker, J. N., Hall, W. P., Lyandres, O., Shah, N. C., Zhao, J., & Van Duyne, R. P. (2009). Biosensing with plasmonic nanosensors. *Nanoscience and Technology: A Collection of Reviews from Nature Journals*, 308–319. https://doi.org/10.1142/9789814287005_0032

Aslan, E., Aslan, E., Turkmen, M., & Saracoglu, O. G. (2017). Metamaterial plasmonic absorber for reducing the spectral shift between near- and far-field responses in surface-enhanced spectroscopy applications. *Sensors and Actuators A: Physical*, *267*, 60–69. https://doi.org/10.1016/j.sna.2017.10.006

Barnes, W. L., Dereux, A., & Ebbesen, T. W. (2003). Surface plasmon subwavelength optics. *Nature 2003 424:6950*, *424*(6950), 824–830. https://doi.org/10.1038/nature01937

Cetin, A. E., Kaya, S., Mertiri, A., Aslan, E., Erramilli, S., Altug, H., & Turkmen, M. (2015). Dual-band plasmonic resonator based on Jerusalem cross-shaped nanoapertures. *Photonics and Nanostructures - Fundamentals and Applications*, *15*, 73–80. https://doi.org/10.1016/j.photonics.2015.04.001

Çetin, A. E., Turkmen, M., Aksu, S., & Altug, H. (2012). Nanoparticle-based metamaterials as multiband plasmonic resonator antennas. *IEEE Transactions on Nanotechnology*, *11*(1), 208–212. https://doi.org/10.1109/tnano.2011.2174160

Cetin, A. E., Turkmen, M., Aksu, S., Etezadi, D., & Altug, H. (2015). Multi-resonant compact nanoaperture with accessible large nearfields. *Applied Physics B: Lasers and Optics*, *118*(1), 29–38. https://link.springer.com/article/10.1007/s00340-014-5950-7

Coskun, A. F., Cetin, A. E., Galarreta, B. C., Alvarez, D. A., Altug, H., & Ozcan, A. (2014). Lensfree optofluidic plasmonic sensor for real-time and label-free monitoring of molecular binding events over a wide field-of-view. *Scientific Reports 2014 4:1*, *4*(1), 1–7. https://doi.org/10.1038/srep06789

Homola, J. (2008). Surface plasmon resonance sensors for detection of chemical and biological species. *Chemical Reviews*, *108*(2), 462–493. https://pubs.acs.org/doi/10.1021/cr068107d

Johnson, P. B., & Christy, R. W. (1972). Optical Constants of the Noble Metals. *Physical Review B*, *6*(12), 4370. https://doi.org/10.1103/PhysRevB.6.4370

Knight, M. W., Sobhani, H., Nordlander, P., & Halas, N. J. (2011). Photodetection with active optical antennas. *Science*, *332*(6030), 702–704. https://www.science.org/doi/10.1126/science.1203056

Lal, S., Link, S., & Halas, N. J. (2007). Nano-optics from sensing to waveguiding. *Nature Photonics 2007 1:11*, *1*(11), 641–648. https://doi.org/10.1038/nphoton.2007.223

López-Tejeira, F., Rodrigo, S. G., Martín-Moreno, L., García-Vidal, F. J., Devaux, E., Ebbesen, T. W., Krenn, J. R., Radko, I. P., Bozhevolnyi, S. I., González, M. U., Weeber, J. C., & Dereux, A. (2007). Efficient unidirectional nanoslit couplers for surface plasmons. *Nature Physics 2007 3:5*, *3*(5), 324–328. https://doi.org/10.1038/nphys584

Maier, S. A. (2007). Plasmonics: Fundamentals and applications. *Plasmonics: Fundamentals and Applications*, 1–223. https://doi.org/10.1007/0-387-37825-1

Mayer, K. M., & Hafner, J. H. (2011). Localized surface plasmon resonance sensors. *Chemical Reviews*, *111*(6), 3828–3857. https://doi.org/10.1021/cr100313v

Nie, S., & Emory, S. R. (1997). Probing Single Molecules and Single Nanoparticles by Surface-Enhanced Raman Scattering. *Science*, *275*(5303), 1102–1106. https://doi/10.1126/science.275.5303.1102

Novotny, L., & Hecht, B. (2006). Principles of nano-optics. *Principles of Nano-Optics*, *9780521832243*, 1–539. https://doi.org/10.1017/cbo9780511813535

Ozbay, E. (2006). Plasmonics: Merging Photonics and Electronics at Nanoscale Dimensions. *Science*, *311*(5758), 189–193. https://doi.org/10.1126/ science.1114849

Schuller, J. A., Barnard, E. S., Cai, W., Jun, Y. C., White, J. S., & Brongersma, M. L. (2010). Plasmonics for extreme light concentration and manipulation. *Nature Materials 2010 9:3*, *9*(3), 193–204. https://doi.org/10.1038/nmat2630

Soler, M., Belushkin, A., Cavallini, A., Kebbi-Beghdadi, C., Greub, G., & Altug, H. (2017). Multiplexed nanoplasmonic biosensor for one-step simultaneous detection of Chlamydia trachomatis and Neisseria gonorrhoeae in urine. *Biosensors and Bioelectronics*, *94*, 560–567. https://doi.org/10.1016/j.bios.2017.03.047

Stewart, M. E., Anderton, C. R., Thompson, L. B., Maria, J., Gray, S. K., Rogers, J. A., & Nuzzo, R. G. (2008). Nanostructured plasmonic sensors. *Chemical Reviews*, *108*(2), 494–521. https://pubs.acs.org/doi/10.1021/cr068126n

Taflove, A., Hagness, S., Engineering, M. P.-M.-T. E., & 2005, undefined. (n.d.). Computational electromagnetics: the finite-difference time-domain method. *Academia.EduA Taflove, SC Hagness, M Piket-MayThe Electrical Engineering Handbook, 2005•academia.Edu*. Retrieved May 20, 2024, from https://www.academia.edu/download/63242042/Electrical_Engineering_Handbook20200508-12748-1318gxz.pdf#page=648

Xu, H., Bjerneld, E. J., Käll, M., & Börjesson, L. (1999). Spectroscopy of Single Hemoglobin Molecules by Surface Enhanced Raman Scattering. *Physical Review Letters*, *83*(21), 4357. https://doi.org/10.1103/PhysRevLett.83.4357

Zia, R., Schuller, J. A., Chandran, A., & Brongersma, M. L. (2006). Plasmonics: the next chip-scale technology. *Materials Today*, *9*(7–8), 20–27. https://doi.org/10.1016/S1369-7021(06)71572-3

CHAPTER II

L6-L7 Vehicles Low Voltage Harness Design

Hicran ALTUNPUL[1]
Alp Tekin ERGENÇ[2]

Introduction

Automotive industry is a dynamic field where technological advancements rapidly influence vehicle design. The increasing popularity of electric and hybrid vehicles has added complexity to the electrical and electronic systems within vehicles, making the design of wiring harnesses more critical. In this context, L6 and L7 class vehicles, which are ideal for urban use and light cargo transportation, highlight the importance of the reliability and efficiency of their electrical systems.

L6 and L7 class vehicles are defined as light commercial vehicles and small-sized vehicles used for urban transportation. These vehicles are known for being user-friendly, environmentally

[1] Student, Yildiz Technical University, altunpulhicran@gmail.com
[2] Associate Prof. Dr, Yildiz Technical University, Orcıd : 0000-0001-6659-7370

friendly, and economical. However, the proper functioning of their electrical and electronic systems is crucial for safe driving and overall vehicle performance. Therefore, the design of wiring harnesses in these vehicles holds significant importance.

Wiring harnesses are critical components in modern vehicles, providing the necessary electrical connections between various parts and systems. According to [S. Olbrich and J. Lackinger, 2022], the complexity and importance of wiring harnesses have grown with the advent of electric and hybrid vehicles, requiring more sophisticated design and manufacturing techniques.

Recent studies (X. Yan, Y. Yan, Y. Li, 2019) have highlighted the need for reliability and efficiency in harness design to ensure vehicle safety and performance.

Methods

In this research, specifications of light vehicles were gathered and requirements were compiled. The vehicle's electrical systems were categorized, and both a pin-out scheme and a concept scheme created.

L6 vehicles are often electrically powered and designed for use in urban areas or restricted environments where speeds are limited. These vehicles are suitable for short-distance commuting within cities or towns, where higher speeds are not necessary. L6 vehicles are typically compact and maneuverable, making them suitable for navigating crowded urban streets and narrow lanes. L6 vehicles are restricted to a maximum speed of around 45 km/h or lower, ensuring safety in urban environments.

L7 vehicles might include specialized light vehicles designed for specific purposes, such as golf carts, utility vehicles, or small delivery vehicles. Similar to L6 vehicles, L7 vehicles are designed for low-speed operation, typically with a maximum speed of around 45 km/h or lower. While many L7 vehicles may be electrically powered for environmental and efficiency reasons, some may still use gasoline or other fuels depending on the application and infrastructure available.

Light electric vehicles are primarily powered by electric motors. The power source can be batteries (such as lithium-ion batteries), fuel cells (for hydrogen-powered vehicles), or a combination of both. Battery capacities may range from around 5 kWh to 20 kWh or more. Larger battery capacities generally provide longer range but can also increase vehicle weight and cost.

Key Factors

Designing a low-voltage harness for electric vehicles, especially for light vehicles like L6 and L7, requires careful consideration of various factors to ensure safety, efficiency, reliability, and compliance with regulations. Here are key factors to consider:

Determine the voltage and current requirements of the electrical system based on the components it will power, such as the motor, lights, sensors, and other electronic systems. For low-voltage systems, typical voltages may range from 12V to 48V, while current requirements depend on the power demands of the components.

Select appropriate wire sizes and materials based on the current-carrying capacity, voltage drop considerations, and environmental factors. Use materials that are suitable for automotive applications, such as copper or aluminum conductors with appropriate insulation to withstand temperature variations, moisture, and vibrations.

Plan the routing of the harness to minimize interference with other vehicle components, avoid sharp bends, and protect the cables from abrasion, heat, and potential damage. Use protective conduit, grommets, and looms to secure and shield the harness from external hazards.

Choose connectors that are compatible with the electrical components and provide secure, reliable connections. Consider factors such as waterproofing, durability, ease of installation, and maintenance requirements.

Ensure that the harness design minimizes electromagnetic interference (EMI) and susceptibility to external interference to prevent malfunctions and ensure the proper operation of electronic systems. Use shielding, grounding, and proper routing techniques to mitigate EMI risks.

Incorporate appropriate fusing and circuit protection devices to safeguard the electrical system against overcurrent conditions, short circuits, and other faults. Use fuses, circuit breakers, or electronic protection modules to prevent damage to components and ensure system reliability.

Coordinate the harness design with other vehicle systems, such as the powertrain, chassis, and body electronics, to ensure

compatibility, optimize performance, and minimize integration challenges during vehicle assembly and testing.

Conduct thorough testing and validation of the harness design to verify electrical continuity, functionality, and reliability under normal and abnormal operating conditions. Perform electrical tests, such as continuity checks, insulation resistance measurements, and voltage drop tests, to ensure compliance with specifications and standards.

Requirements & Standards

Homologation limits for low voltage harnesses, may vary depending on regulatory requirements in different regions and countries.

Electrical Safety Standards

Low-voltage harnesses must meet specific insulation resistance requirements, typically measured in ohms per unit length. This ensures that the insulation materials effectively isolate conductors and prevent electrical leakage or short circuits.

The dielectric strength of insulation materials should be sufficient to withstand high voltage levels without breakdown. This property is crucial for ensuring electrical safety and preventing insulation failures.

Voltage drop along the length of the harness should be within acceptable limits to ensure that electrical components receive the required voltage for proper operation. This requires careful consideration of conductor size, material resistance, and circuit design.

Electromagnetic Compatibility (EMC) Regulations

Low-voltage harnesses must limit conducted emissions, which are electrical disturbances transmitted through the wiring harness. This requires filtering and suppression techniques to reduce noise and interference.

Harnesses should minimize radiated emissions, which are electromagnetic waves emitted by the wiring harness. Shielding and grounding techniques may be employed to contain and mitigate radiated emissions.

Low-voltage harnesses must demonstrate immunity to external electromagnetic interference, such as electromagnetic fields generated by nearby electronic devices or electromagnetic radiation from radio frequency (RF) sources. Shielding, grounding, and filtering techniques are used to improve immunity.

Environmental Regulations

Insulation materials used in low-voltage harnesses should have temperature ratings suitable for automotive applications, typically ranging from -40°C to 125°C or higher. This ensures reliable performance under extreme temperature conditions.

Harnesses must resist moisture ingress to prevent corrosion and electrical short circuits. This may involve using moisture-resistant insulation materials, sealing connectors, and employing protective sheathing.

Harness materials should be resistant to automotive fluids, such as oils, fuels, and cleaning agents, to ensure long-term reliability and performance in harsh operating environments.

Quality and Reliability Standards

Manufacturers must maintain traceability of materials used in low-voltage harnesses to ensure compliance with specifications and regulatory requirements. This involves tracking material sources, batch numbers, and certification documents.

Harness assembly processes must be carefully controlled to ensure consistent quality and reliability. This includes techniques such as crimping, soldering, and heat-shrinking connectors, as well as automated testing and inspection.

Low-voltage harnesses undergo various reliability tests, including thermal cycling, vibration testing, mechanical stress testing, and accelerated aging tests, to ensure durability and long-term performance in real-world conditions.

Voltage Drop

Voltage drop is a crucial consideration in the design of low voltage harnesses for automotive applications, including L6 and L7 vehicles. It refers to the decrease in voltage that occurs as electrical current flows through the conductors of the harness. Excessive voltage drop can lead to diminished performance of electrical components, reduced efficiency, and potential safety hazards.

Voltage drop occurs due to the inherent resistance of the conductive materials used in the harness, including wires, connectors, and terminals.

Factors contributing to voltage drop include the length and gauge of the conductors, the material properties of the conductors (e.g., resistivity), and the quality of connections between components. Voltage drop can be calculated using Ohm's Law,

which states that voltage drop (V) equals current (I) multiplied by resistance (R), expressed as $V = I \times R$. The resistance of the conductors can be determined based on factors such as wire gauge, material properties, and length of the conductor. Voltage drop calculations consider the maximum allowable voltage drop specified for the electrical system and the operating conditions of the vehicle. Excessive voltage drop can result in reduced voltage levels reaching electrical components, affecting their performance and functionality.

In automotive applications, voltage drop can lead to dimming of lights, reduced motor performance, slower operation of electronic devices, and potential damage to sensitive components. Voltage drop may also result in increased power dissipation in the conductors, leading to heating and potential safety hazards, particularly in high-current circuits. Design considerations to mitigate voltage drop include using conductors with appropriate gauge sizes to minimize resistance, reducing the length of wiring harnesses where possible, and optimizing routing to minimize voltage drop.

Additionally, ensuring secure and low-resistance connections between components, including terminals, connectors, and splices, helps to minimize voltage drop. Voltage drop can also be reduced by using materials with lower resistivity, such as high-conductivity copper or aluminum alloys, and employing techniques such as parallel conductor runs or busbars to distribute current more effectively.

Pin-out Schematics

The TMC(motor controller) is the core component, interfacing with the power supply, battery, sensors, and display. The pinout provides specific details for connecting wires to the TMC, ensuring all components communicate correctly. This setup is critical for managing the system, ensuring efficient and safe vehicle operation.

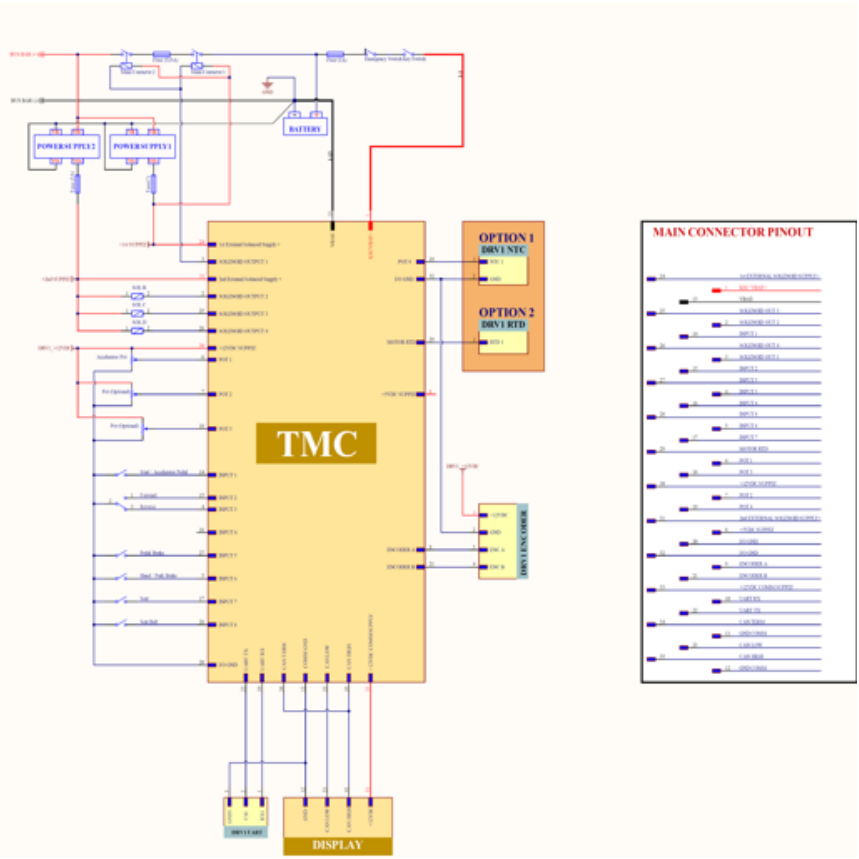

Figure 1 Pin-out Schematics of TMC

Power Connections

The battery is connected to the PSUs(Power Supply Unit), which then connect to the TMC(motor controller). Red line indicate power supply (12V or 24V in automotive applications).

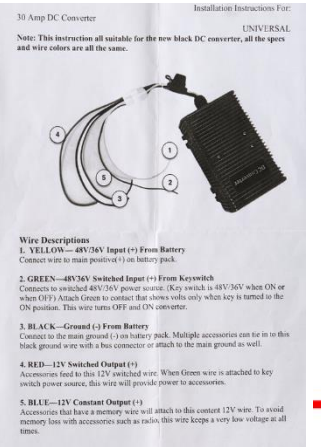

Figure 2 DC Converter Connections

TMC Connections

Inputs (Left Side)

Various inputs such as sensor data, brake signals, and other control inputs are connected here. These inputs are critical for the TMC to manage based on real-time data.

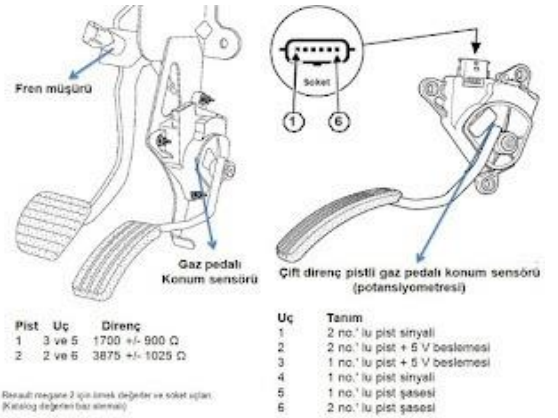

Figure 3 Brake and accelerator pedal connections

Outputs (Right Side)

Outputs to the display other actuators or systems in the vehicle.

Figure 4 Inverter and Electric Motor

Display Connection

Direct connection from the TMC to the display unit. This connection likely includes both power and data lines to operate the display and transmit information.

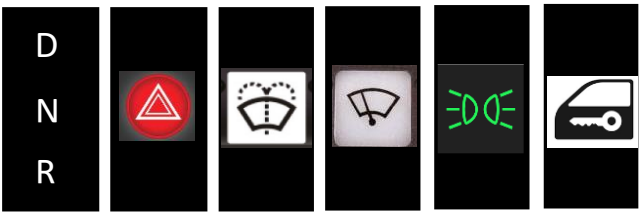

Figure 5 Display icons

Main Connector Pinout

Each pin has a specific function, such as power input, ground, sensor inputs, and signal outputs. Pinout helps in understanding which wire connects to which part of the system, ensuring proper installation and troubleshooting.

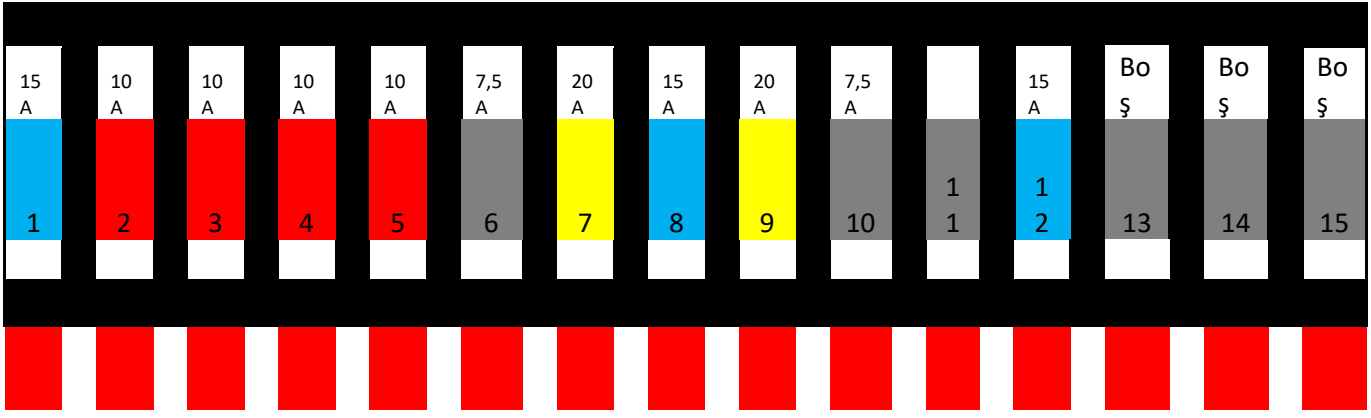

Figure 6 Main Connector Pin-out

Key Signals

12V_DC_1 and 12V_DC_2

These are power supply lines coming from the power supplies (PSU1 and PSU2) to the TMC.

Ground Connections

Essential for completing the electrical circuit and ensuring stable operation of the electronic components.

Sensor Inputs (e.g., CDC)

Inputs from various sensors, like brake sensors, that provide data to the TMC for processing.

These inputs help the TMC make decisions about how to control the transmission.

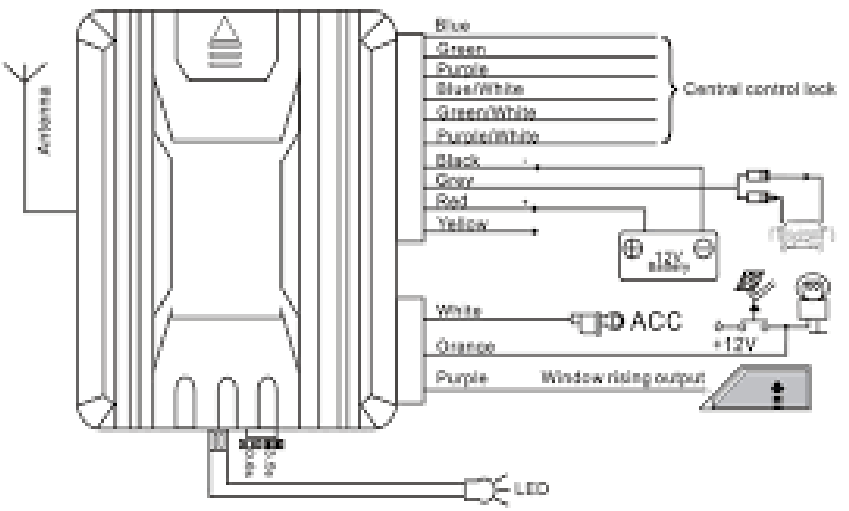

Figure 7 Central Door Controller

Data and Control Lines

Lines that carry data and control signals between the TMC and other components (like the display and optional brake components). Ensure the TMC can send and receive information to operate the transmission system effectively.

Since the electronic components in the braking system are standard, no calculation has been done; only the sensors are selected. In the lighting system, to extend the life of the LV battery, LEDs are used at the rear. Cheaper and longer-lasting choices has been made.

Conclusions

The research highlighted the significant shifts in transportation behavior prompted by the COVID-19 pandemic, emphasizing the growing trend towards micro-mobility solutions. As urban commuters increasingly opt for environmentally friendly and efficient alternatives, electric L-category vehicles have emerged as a promising solution. These vehicles, characterized by their compact size, lightweight design, and lower energy requirements, offer advantages such as cost-effective production and faster recharging times.

In addressing the homologation and electrification requirements of these vehicles, this study underscores the critical role of properly designed wiring harnesses in ensuring safe and efficient vehicle operation. Key factors in harness design, such as voltage and current requirements, material selection, routing, connectors, electromagnetic interference management, and fusing, are essential to meet regulatory standards and ensure reliability.

By categorizing the vehicle's electrical systems and developing comprehensive pin-out and concept schemes, the study provides a foundation for the implementation of electric L-category vehicles. These vehicles not only contribute to reducing emission and noise pollution but also align with the evolving preferences of urban commuters for convenient, sustainable transportation solutions. Ultimately, this research supports the advancement of light electric vehicles as viable alternatives for personal mobility, highlighting their potential to enhance urban transportation dynamics.

References

1. Olbrich S., Lackinger J., (2022), Manufacturing Processes of automotive high-voltage wire harnesses, 55th CIRP Conference on Manufacturing Systems.
2. Xinxing Y., Yu Y., Yuqing L., (2019), Design and application of low cost and high reliability intelligent electric vehicle overall wire harness, AIP Conference Proceedings 2154.

CHAPTER III

Design of a Titanium Nitride-Based Metasurface for 30 Degree Deflection at 1550 nm

Yunus UÇAR[1]
Ekin ASLAN[2]
Erdem ASLAN[3]

Introduction

Metasurfaces, composed of arrays of subwavelength scatterers, have revolutionized the field of optics by enabling precise control over light propagation (Zheludev & Kivshar, 2012). Unlike traditional optical components, which rely on bulk materials to manipulate light, metasurfaces operate at the nanoscale, allowing

[1] PhD Student, Kayseri University, Faculty of Engineering, Architecture and Design, Department of Electrical and Electronics Engineering, Kayseri/Türkiye, Orcid: 0000-0002-9174-4202, yunusucar@kayseri.edu.tr
[2] Assoc. Prof, Kayseri University, Faculty of Engineering, Architecture and Design, Department of Electrical and Electronics Engineering, Kayseri/Türkiye, Orcid: 0000-0003-0933-7796, ekinaslan@kayseri.edu.tr
[3] Assoc. Prof, Erciyes University, Faculty of Engineering, Department of Electrical and Electronics Engineering, Kayseri/Türkiye, Orcid: 0000-0001-6829-9000, aslanerdem@erciyes.edu.tr

for tailored manipulation of phase, amplitude, and polarization (Kildishev et al., 2013). The concept of metasurfaces has its roots in metamaterials research, where artificial structures are engineered to exhibit exotic electromagnetic properties (Smith et al., 2004). Metasurfaces offer advantages such as miniaturization, ease of fabrication using standard lithography techniques, and compatibility with existing optical systems (Ni et al., 2013).

Metasurfaces, comprising an array of sub-wavelength nanostructures, can be conceptualized as a grid of discrete elements analogous to the pixels of a phase (and possibly amplitude) mask (Scheuer, 2017). This foundational notion is elucidated in Figure 1, where a flat surface is discretized into distinct pixels. Each pixel imposes a distinct local phase shift denoted by $\emptyset_{ij}$, collectively delineating a discretized rendition of a phase map, $\emptyset(x, y)$. This phase profile elucidates the requisite phase distribution necessary for attaining the desired beam morphology (Scheuer, 2017). These metasurfaces, in addition to their role in shaping optical wavefronts, also hold promise in enabling compact and lightweight optical devices, thereby revolutionizing various fields including imaging, sensing, and communication.

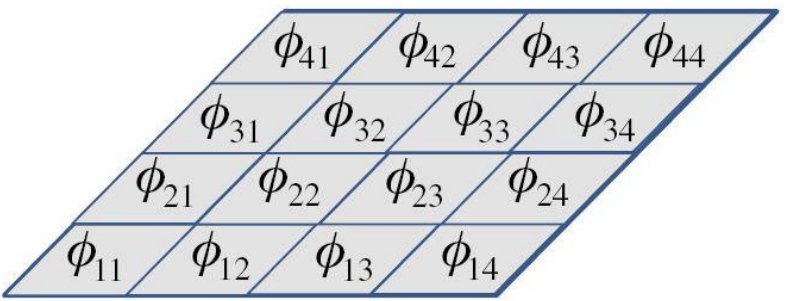

Figure 1: Phase Diagram of Metasurface (Scheuer, 2017).

After the incident beam interacts with the metasurface, either by reflection or transmission, and propagates a distance z, its surface field profile can be described by the Kirchhoff integral:

$$U_z(x,y) = e^{i\frac{\pi}{\lambda z}(x^2+y^2)} \iint U_0(\xi,\eta)\, e^{i\frac{\pi}{\lambda z}(\xi^2+\eta^2)++\, i\emptyset(\xi,\eta)} \exp\left[-i\frac{2\pi}{\lambda z}(\xi x + \eta y)\right] d\xi d\eta \quad (1)$$

In this context, U_0 stands for the initial field profile of the incident beam, while λ represents the wavelength, and U_z indicates the field profile at a distance z from the metasurface. The design of metasurfaces for applications such as beam shaping and holography poses two significant challenges: first, creating the proper phase mask needed to achieve the desired beam shape, and second, engineering the individual nanostructures to deliver specific phase shifts between 0 and 2π. (referred to as the pixels) (Scheuer, 2017).

The principal challenge encountered in the utilization of metasurfaces for precise phase control and beam shaping resides in the imperative to achieve arbitrary phase shifts within the interval [0, 2π], while simultaneously ensuring a consistent amplitude response. To address these exigencies, a plethora of techniques and methodologies have been devised and experimentally validated. These approaches harness a spectrum of mechanisms, encompassing plasmonic and dielectric resonances, cross-polarization interactions, coupled nano-antennas, geometric phase modulation, and related methodologies.

Recent research has explored the use of materials such as titanium nitride (TiN) in metasurface designs. TiN exhibits intriguing optical characteristics, such as a high refractive index and low absorption in the visible and near-infrared spectral ranges

(Valour et al., 2021). Hence, by incorporating TiN into metasurface structures, enhanced light-matter interactions have been achieved and device performance has been (Altug & Vučković, 2005).

Beam deflection in metasurfaces plays a crucial role in various optical systems, including imaging, communication, and sensing (Díez et al., 2011). Traditional beam steering approaches often suffer from limitations such as bulkiness, limited field of view, and slow response times (Ni et al., 2015). Metasurface-enabled beam deflection provides a promising solution by allowing for agile and compact steering of optical beams (Arbabi et al., 2017). The underlying principle involves tailoring the phase profile across the metasurface to achieve the desired beam direction (Aieta et al., 2012). This phase modulation can be achieved by designing subwavelength scatterers with specific geometries and material properties. The following formula illustrates the phase modulation achieved by a metasurface:

$$\Phi(x, y) = k.\emptyset(x, y) \quad (2)$$

where $\Phi(x, y)$ is the phase modulation across the metasurface, k is the wavevector of the incident light, and $\emptyset(x, y)$ is the desired phase profile imposed by the metasurface.

The movement of light in metasurfaces is governed by generalized Snell's laws, which describe the link between the angle of incidence, angle of refraction, and refractive indices of the materials involved (Yu et al., 2011). For metasurfaces, these laws can be extended to account for the tailored phase profile imposed by the subwavelength scatterers. The generalized Snell's law for metasurfaces can be expressed as:

$$n_1 \sin(\theta_1) = n_2 \sin(\theta_2) + \frac{\lambda}{\Lambda} \frac{d\Phi}{d\theta} \tag{3}$$

where n_1 and n_2 are the refractive indices of the incident and refracted media, respectively, θ_1 and θ_2 are the incident and refracted angles, respectively, λ is the wavelength of light, Λ is the period of the metasurface, and $\frac{d\Phi}{d\theta}$ is the gradient of the phase profile across the metasurface.

In addition to generalized beam deflection, metasurfaces can achieve x-deflection and y-deflection by imparting different phase profiles along orthogonal axes (Yu et al., 2011). The x-deflection and y-deflection angles can be controlled independently by designing the metasurface structure accordingly. The formulas for x-deflection and y-deflection are given by:

$$\theta_x = \frac{\lambda}{\Lambda} \frac{d\Phi}{dx} \tag{4}$$

$$\theta_y = \frac{\lambda}{\Lambda} \frac{d\Phi}{dy} \tag{5}$$

where θ_x and θ_y are the x-deflection and y-deflection angles, respectively, $\frac{d\Phi}{dx}$ and $\frac{d\Phi}{dy}$ are the gradients of the phase profile along the x and y axes, respectively.

Recent advancements in metasurface-enabled beam deflection have opened up exciting possibilities in a wide range of applications, including augmented reality displays, LiDAR systems, and optical communication (Khorasaninejad et al., 2016).

Dynamic metasurfaces, which can be reconfigured in real-time, offer enhanced functionality for applications such as beam shaping and adaptive optics (Fischer et al., 2011). The integration of metasurface devices into integrated photonic circuits holds promise for realizing compact and multifunctional optical systems (Verslegers et al., 2009). Moreover, advances in nanofabrication techniques, such as electron beam lithography and focused ion beam milling, have facilitated the fabrication of complex metasurface structures with subwavelength features (Yu et al., 2011).

In this study, an alternative TiN-based plasmonic-based metasurface design that can perform beam deflection at an operating wavelength of 1550 nm is proposed. In order to achieve deflective metasurfaces, it is necessary to provide a specific interfacial phase distribution on the metasurface, depending on the desired deflection angle. For this particular metasurface design, which can reflect at 30° deflection, the necessary interfacial phase distribution is first determined. Subsequently, a set of unit cells with various geometries and geometric parameters, exhibiting 18 different phase values in the [0-2π] range in this phase distribution, is theoretically designed. Each nanoantenna designed for effective beam deflection must provide this phase distribution with the highest possible resolution. Thus, the number of meta-cells that will provide much higher phase resolution compared to the studies presented in the literature is obtained. The reflection characteristic and phase responses of these unit cells at 1550 nm are analyzed using the Finite-Difference Time-Domain (FDTD) method. Dielectric permittivity data of TiN layers are obtained from ellipsometric data of a TiN film deposited at 800°C using the

Drude-Lorentz model and imported into numerical analyses. While the periodic arrays of each antenna are analyzed separately, their phase and reflectance values are determined using field monitors. Finally, the aperiodic arrangement of these antennas on the interface is designed by taking into account the phase distribution of the relevant deflector metasurface and analyzes are carried out to reveal the deflector feature.

Method

In this study, a metasurface design capable of deflecting beams at a specific θ_0 angle through alternative plasmonic meta-cells is presented. In this context, in order for deflection to be achieved on the plane of incidence of light, the phase pattern that needs to be created on the sample surface must satisfy the following equation.

$$\varphi_m(x,\lambda) = -\frac{2\pi}{\lambda}\sin(\theta_0)\,x \tag{6}$$

The phase shift φ_m in the equation represents the phase displacement, and θ_0 represents the deflection angle of the reflected light.

According to this equation, in order to achieve a beam deflection of $\theta_0 = 30°$, the meta-cell arrangements must be provided according to the phase map shown in Figure 2. Here, a 800 μm × 800 μm meta-cell array is proposed for this purpose. To achieve this, different meta-cell designs must be conceived for each distinct phase cell. In the meta-cell analyses for a beam deflection application where the plane of incidence is xz and the direction of deflection is along x, the analyzed cells are illuminated with x -

linearly polarized light along the x -direction. Schematic representations of the designed meta-cells are given in Figures 3 and 4. Accordingly, each meta-cell is configured sequentially with a TiN reflective layer, an SiO_2 transmissive intermediary layer, and a TiN nanoantenna layer. Such nanostructures are absorptive structures with significant reflection resonances (Aslan et al., 2017). Hence, they are suitable structures for efficiently deflecting the reflected light.

The nanoantenna layer consists of two different types of geometric structures. By adjusting the geometric parameters of these structures, various electromagnetic phase responses can be achieved within the range of 0-2π. The trial version of the commercial Ansys Lumerical software, utilizing the FDTD method, is employed to determine the electromagnetic phase responses and reflection characteristics of the meta-cell (*Optical Simulation and Design Software | Ansys Optics*, n.d.). The operational wavelength is set to 1550 nm, falling within the fiber optic wavelength spectrum. The 1550 nm wavelength is widely used in fiber optic communication due to its low loss and low dispersion characteristics.

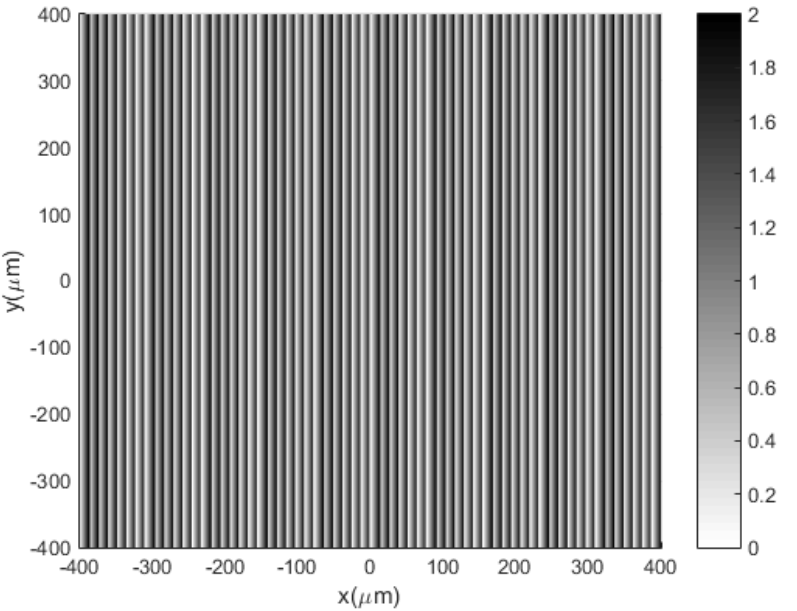

Figure 2: Intended Metasurface Phase Map in π.

The specific values of Drude-Lorentz parameters can vary for each material and are often provided in scientific research articles. In the study conducted by (Naik et al., 2013), Drude-Lorentz parameters for several alternative plasmonic materials, including TiN have been determined using equation 7 for the wavelengths ranging from 350 to 2000 nm (Naik et al., 2013).

$$\varepsilon(\omega) = \varepsilon_b - \frac{\omega_p^2}{\omega\left(\omega + i\gamma_p\right)} + \frac{f_1\omega_1^2}{\left(\omega_1^2 - \omega^2 - i\omega\gamma_1\right)} \tag{7}$$

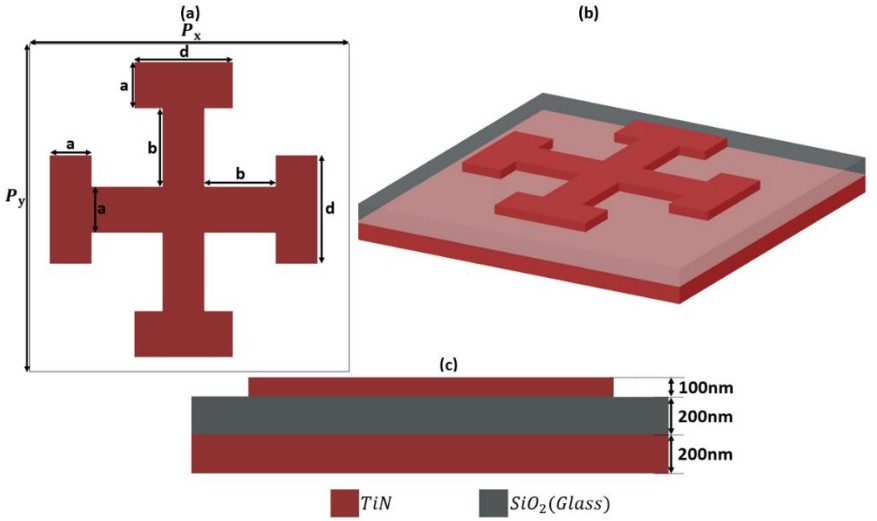

Figure 3: The Designed Jerusalem Cross Shape Antenna Structure: (a) top view, (b) perspective and (c) side views.

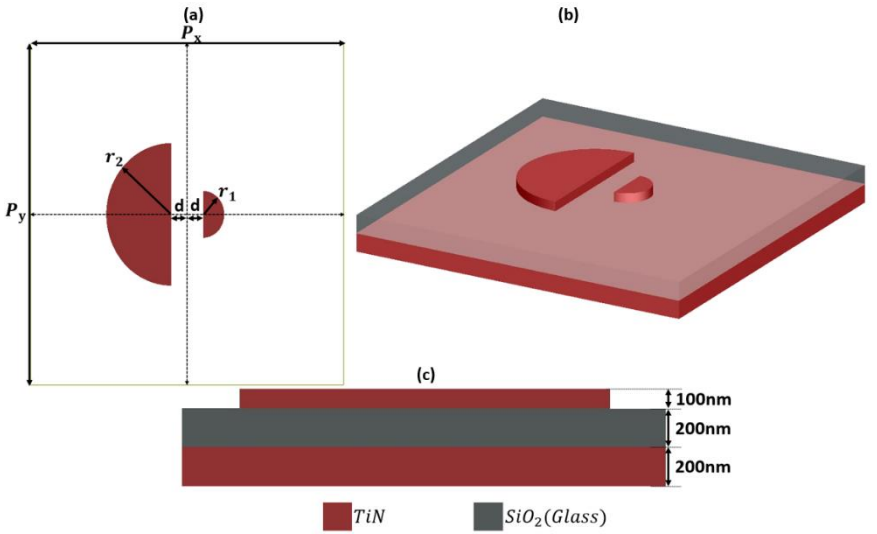

Figure 4: The Designed Semi-Circle Couple Shape Antenna Structure: (a) top view, (b) perspective and (c) side views.

In Equation 7, the second term represents the Drude model, and the third term represents the Lorentz Oscillator. The term ε_b in the equation represents the polarization response from the core electrons, ω_p is the plasma frequency, γ_p is the carrier relaxation rate, f_1 is the strength of the Lorentz oscillator, ω_1 is the central frequency of the Lorentz oscillator, and γ_1 represents the damping of the Lorentz oscillator. The TiN data used in the study were obtained using values of $\varepsilon_b = 4.855$, $\omega_p = 7.9308$, $\gamma_p = 0.1795$, $f_1 = 3.2907$, $\omega_1 = 4.2196$, and $\gamma_1 = 2.0341$ for TiN deposited at 800°C (Naik et al., 2013). The SiO_2 data used in the study is available in the library of Ansys Lumerical software.

Results and Discussion

In the meta-cell analysis, the phase and reflection responses are examined. Table 1 presents the phase and reflection responses of meta-cells with antenna layers in various geometrical parameters, showing a very smooth phase change within 0-2π range. Figures 5 and 6 illustrate the phase and reflection responses of these antennas based on antenna number. While the phase loss can be effectively achieved quite, the reflection remains at approximately 0.7 on average.

Table 1: Geometric Parameters of Designed Antenna Array.

Antenna No	Antenna Type	Geometric Parameters								
		Reflection	**Phase (π)**	**a (nm)**	**b (nm)**	**d (nm)**	**r_1 (nm)**	**r_2 (nm)**	**Px (nm)**	**Py (nm)**
1	Jerusalem Cross	0,6699	0,0232	250	200	450	-	-	2500	2500
2	Jerusalem Cross	0,7378	0,1247	200	350	750	-	-	2500	2500
3	Jerusalem Cross	0,5940	0,2449	200	300	500	-	-	2500	2500
4	Jerusalem Cross	0,7442	0,3440	250	450	800	-	-	2500	2500
5	Jerusalem Cross	0,7383	0,4425	300	450	850	-	-	2500	2500
6	Jerusalem Cross	0,6853	0,5485	300	450	1000	-	-	2500	2500
7	Jerusalem Cross	0,7857	0,6492	300	450	550	-	-	2500	2500
8	Jerusalem Cross	0,7889	0,7472	250	350	600	-	-	2500	2500
9	Jerusalem Cross	0,7738	0,8438	200	400	600	-	-	2500	2500
10	Jerusalem Cross	0,7685	0,9448	200	400	650			2500	2500
11	Semi-Circle Couple	0,7316	1,2588	-	-	250	500	500	2500	2500
12	Jerusalem Cross	0,7410	1,3411	200	500	700	-	-	2500	2500
13	Semi-Circle Couple	0,8487	1,4383	-	-	125	100	475	2500	2500
14	Jerusalem Cross	0,7418	1,5316	200	400	700	-	-	2500	2500
15	Semi-Circle Couple	0,8314	1,6582	-	-	125	175	525	2500	2500
16	Jerusalem Cross	0,7426	1,7545	200	250	350	-	-	2500	2500
17	Jerusalem Cross	0,7384	1,8679	200	350	700	-	-	2500	2500
18	Jerusalem Cross	0,6681	1,9512	200	250	500	-	-	2500	2500

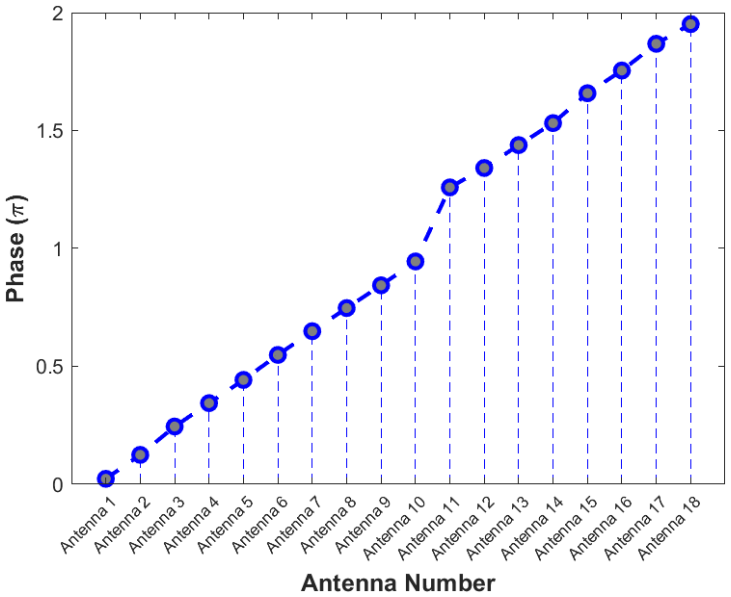

Figure 5: Antenna Phase Values.

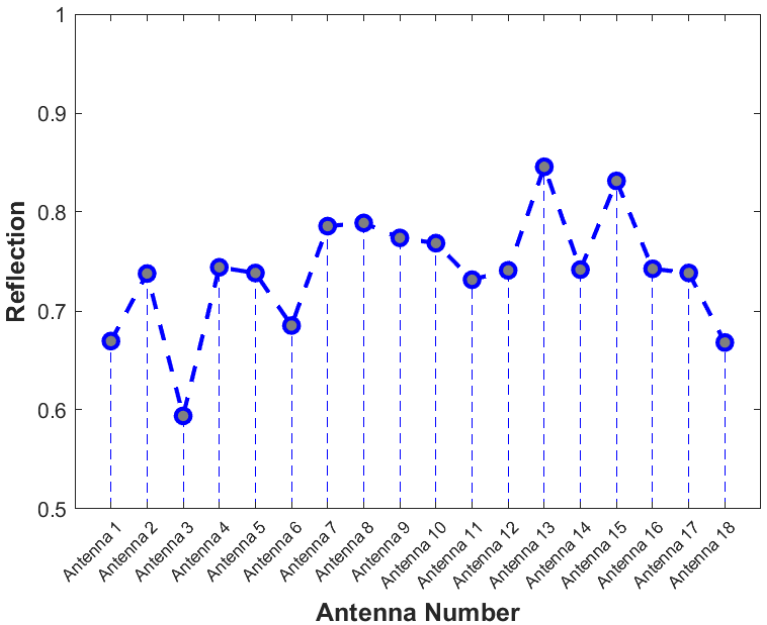

Figure 6: Antenna Reflection Values.

In the literature (Guo et al., 2018; Xu et al., 2019; Yu & Capasso, 2014), studies on phase analysis with a maximum resolution of 8 antennas have been found. In this study, a phase resolution of 18 antennas could be achieved. Furtermore, a deflection angle of 30° has been achieved as can be observed from Figure 7, where k_r is the wavevector of the reflected light.

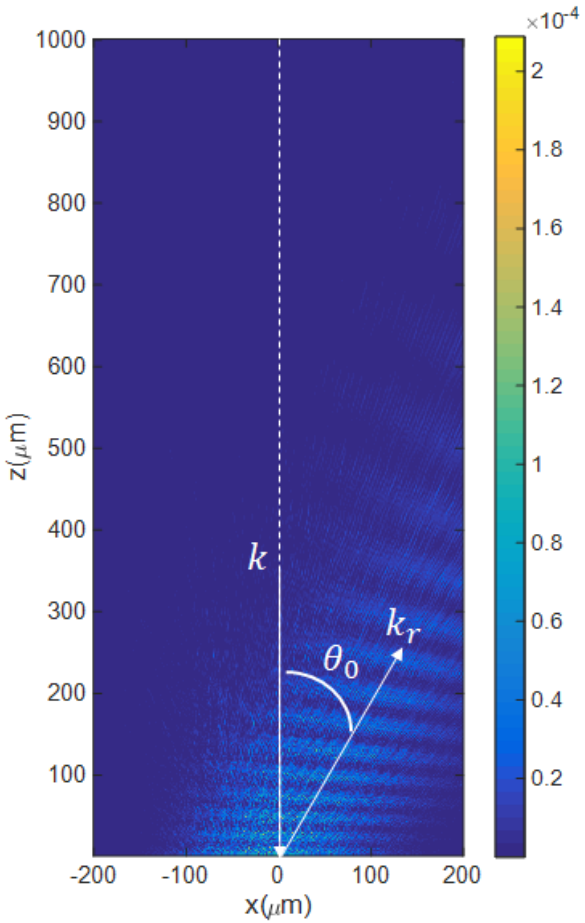

Figure 7: The Theoretical Beam Deflection Characteristic of the Proposed Metasurface Design.

Conclusion

In this study, meta-cell designs that provide high-resolution phase transition have been made. The necessary metasurface phase map for these meta-cells to perform 30° beam deflection has been determined, and the aperiodic arrangements that fit this phase map have also been analyzed. As a result of these analyses, the deflection outcome of the proposed metasurface design is presented. Based on this outcome, the expected 30° deflection could theoretically be achieved. Since the reflection values are not exactly 1, it is an expected result that unwanted scattering or interference cause deviation from the targeted deflection direction. A more effective deflection can be achieved when a good and stable reflection as well as a good phase response are attained.

Acknowledgement

This study was supported by Scientific and Technological Research Council of Turkey (TUBITAK) under the Grant Number 121E518. The authors thank to TUBITAK for their supports

References

Aieta, F., Genevet, P., Kats, M. A., Yu, N., Blanchard, R., Gaburro, Z., & Capasso, F. (2012). Aberration-free ultrathin flat lenses and axicons at telecom wavelengths based on plasmonic metasurfaces. *Nano Letters*, *12*(9), 4932–4936.

Altug, H., & Vučković, J. (2005). Experimental demonstration of the slow group velocity of light in two-dimensional coupled photonic crystal microcavity arrays. *Applied Physics Letters*, *86*(11).

Arbabi, A., Arbabi, E., Horie, Y., Kamali, S. M., & Faraon, A. (2017). Planar metasurface retroreflector. *Nature Photonics 2017 11:7*, *11*(7), 415–420.

Aslan, E., Aslan, E., Turkmen, M., & Saracoglu, O. G. (2017). Experimental and numerical characterization of a mid-infrared plasmonic perfect absorber for dual-band enhanced vibrational spectroscopy. *Optical Materials*, 73, 213-222.

Díez, A., Andrés, M. V., Silvestre, E., Cascante-Vindas, J., Velázquez-Ibarra, L., Abreu-Afonso, J., ... & Lucio, J. L. (2011, October). Tailoring the dispersion of photonic crystal fibers for supercontinuum and photon pairs generation. In *22nd Congress of the International Commission for Optics: Light for the Development of the World* (Vol. 8011, pp. 824-829). SPIE.

Fischer, J., Ergin, T., & Wegener, M. (2011). Three-dimensional polarization-independent visible-frequency carpet invisibility cloak. *Optics letters*, *36*(11), 2059-2061.

Guo, Z., Xu, H., Guo, K., Shen, F., Zhou, H., Zhou, Q., ... & Yin, Z. (2018). High-efficiency visible transmitting polarizations devices based on the GaN metasurface. *Nanomaterials*, *8*(5), 333..

Khorasaninejad, M., Chen, W. T., Devlin, R. C., Oh, J., Zhu, A. Y., & Capasso, F. (2016). Metalenses at visible wavelengths: Diffraction-limited focusing and subwavelength resolution imaging. *Science*, *352*(6290), 1190–1194.

Kildishev, A. V., Boltasseva, A., & Shalaev, V. M. (2013). Planar photonics with metasurfaces. *Science*, *339*(6125), 1232009.

Naik, G. V., Shalaev, V. M., & Boltasseva, A. (2013). Alternative Plasmonic Materials: Beyond Gold and Silver. *Advanced Materials*, *25*(24), 3264–3294.

Ni, X., Kildishev, A. V., & Shalaev, V. M. (2013). Metasurface holograms for visible light. *Nature communications*, *4*(1), 2807.

Ni, X., Wong, Z. J., Mrejen, M., Wang, Y., & Zhang, X. (2015). An ultrathin invisibility skin cloak for visible light. *Science*, *349*(6254), 1310–1314.

Optical Simulation and Design Software | Ansys Optics. (n.d.). Retrieved May 15, 2024, from https://www.ansys.com/en-us/products/optics

Scheuer, J. (2017). Metasurfaces-based holography and beam shaping: Engineering the phase profile of light. *Nanophotonics*, *6*(1), 137–152.

Smith, D. R., Pendry, J. B., & Wiltshire, M. C. K. (2004). Metamaterials and Negative Refractive Index. *Science*, *305*(5685), 788–792.

Valour, A., Higuita, M. A. U., Guillonneau, G., Crespo-Monteiro, N., Jamon, D., Hochedel, M., ... & Jourlin, Y. (2021). Optical, electrical and mechanical properties of TiN thin film obtained from a TiO2 sol-gel coating and rapid thermal nitridation. *Surface and Coatings Technology*, *413*, 127089.

Verslegers, L., Catrysse, P. B., Yu, Z., White, J. S., Barnard, E. S., Brongersma, M. L., & Fan, S. (2009). Planar lenses based on nanoscale slit arrays in a metallic film. *Nano Letters*, *9*(1), 235–238.

Xu, Y., Li, Q., Zhang, X., Wei, M., Xu, Q., Wang, Q., Zhang, H., Zhang, W., Hu, C., Zhang, Z., Zhang, C., Zhang, X., Han, J., & Zhang, W. (2019). Spin-Decoupled Multifunctional Metasurface for Asymmetric Polarization Generation. *ACS Photonics*, *6*(11), 2933–2941.

Yu, N., & Capasso, F. (2014). Flat optics with designer metasurfaces. *Nature Materials*, *13*(2), 139–150.

Yu, N., Genevet, P., Kats, M. A., Aieta, F., Tetienne, J. P., Capasso, F., & Gaburro, Z. (2011). Light propagation with phase discontinuities: Generalized laws of reflection and refraction. *Science*, *334*(6054), 333–337.

Zheludev, N. I., & Kivshar, Y. S. (2012). From metamaterials to metadevices. *Nature Materials*, *11*(11), 917–924.

CHAPTER IV

Deep Learning-Based Classification Framework For Colon Cancer Detection in Histopathological Images

Rukiye UZUN ARSLAN[1]
Ceren KAYA[2]
Irem SENYER YAPICI[3]

Introduction

Cancer is an important health problem with ever increasing incidence and mortality rates not only in Turkey but also in the worldwide (Siegel et al., 2020; Pavlopoulou, Spandidos & Michalopoulos, 2015). According to the World Health Organization statistics report, cancer is the second prominent cause of death across the world, and it is accountable for an approximate more than 9 million deaths, composing one-sixth of all human

[1] Assoc. Prof. Dr., Zonguldak Bulent Ecevit University, Faculty of Engineering, Department of Electrical and Electronics Engineering, Zonguldak/Turkey, Orcid: 0000-0002-2082-8695, rukiyeuzun67@gmail.com
[2] Asst. Prof. Dr., Zonguldak Bulent Ecevit University, Faculty of Engineering, Department of Biomedical Engineering, Zonguldak/Turkey, Orcid: 0000-0002-1970-2833, crnkaya@hotmail.com
[3] Asst. Prof. Dr., Zonguldak Bulent Ecevit University, Faculty of Engineering, Department of Computer Engineering, Zonguldak/Turkey, Orcid: 0000-0003-0655-340X, senyerirem@gmail.com

deaths in 2018 (Subramanian et al., 2020). Colorectal cancer (CRC) reckons for about 10% of all cancers diagnosed yearly and cancer-related deaths worldwide (Bray et al., 2018). It is the most prevalent cancer type ranked second in women and third in men worldwide, respectively. According to the Public Health Agency of Turkey report, it has been reported as the third most common type of cancer in men and women in our country (THSK, 2023).

Although the cause of colorectal cancer is not known exactly, it has been reported that factors such as age, colorectal polyps, genetic predisposition, lifestyle, and dietary habits increase the likelihood of developing the disease. On the other hand, it is one of the most curable cancers when diagnosed and treated in early stages. Histopathological examination, denominated "gold standard", is one of the most common and trustworthy method used to diagnose CRC. In this method, professional pathologists visually observe organizational changes in cell morphology and tissue components through microscope with the intention of determination of the type and degree of the lesion. However, manual examination possesses certain disadvantages such as requiring experienced pathologists, laborious, long inspection period, observer biases (Abdelsamea et al., 2019; Graham et al., 2019). Hence, it results in need of development of computer-aided detection (CAD) systems with two major aiming, automated segmentation and classification (Kassani et al., 2022).

In this context, artificial intelligence techniques such as deep learning (DL) have been recently used which are well known with their capacities to examine data faster and give decisions. There have been many studies performed based DL to detect

colorectal and lung cancers in literature. For instance, Wang et al. (2019) classified histopathological images of lung cancer with convolutional neural network (CNN) based cell segmentation approach. Hatuwal and Thapa (2020) conducted classification of lung cancer pathological images into three classes with CNN. Nishio et al. (2021) handled the classification of three-class lung cancer pathological images using homology-based image processing methods. Teramoto et al. (2017) proposed a novel deep convolutional neural network method to classify lung tumors by examining their pathological images. Masud et al. (2021) classified lung and colon microscopic images with DL-based supervised learning approach. Togacar (2021) managed to detect five classes of histopathological images including three lung cancer classes and two colorectal cancer classes using CAD model and optimization approaches. Gessert et al. (2019) examined the practicability of colorectal cancer classification in microscopic images using CNNs based on multi-transfer learning approaches. Vuong et al. (2020) regulated to detect colon cancer grading by applying a learning approach analyzed the digitized pathology images where classification and regression task combined with CNN.

In this study, automatic CAD classification of colon cancer is proposed by applying histopathological images to deep pre-trained convolutional neural network (CNN) based InceptionV3 and DenseNet201 models. For this purpose, the classification performances of colon cancer are compared by applying different batch sizes and epoch number values to InceptionV3 and DenseNet201 models.

The remainder of this study is organized as follows. In Section 2, the dataset used in the study and the details of proposed deep learning models are presented. Experimental analyzes and obtained results are given in Section 3. Finally, the study is concluded in Section 4.

2. Material and Method

In this study, deep neural network models based on InceptionV3 and DenseNet201 are used to detect colon cancer from histopathological images. In this direction, firstly, the images in the data set are resized. Then, the data set is expanded with the data augmentation process in order to present more examples to the network. It is then presented to the network to be trained. In the next step, the pooling process is applied between the layers to reduce the splitting and size in the network. Thus, a smaller sized matrix is obtained. Batch normalization is used to reduce the dependence of the model on the data. As the learning algorithm, adaptive moment estimation (Adam) algorithm, which is known to have the best performance in reaching the optimum solution, is preferred (Uckuner & Erol, 2021). Block diagram of proposed deep neural network-based model for the classification of colon cancer from histopathological images are illustrated in Figure 1. Finally, colon adenocarcinoma and colon benign cancers are detected by classifying images through fully connected layers.

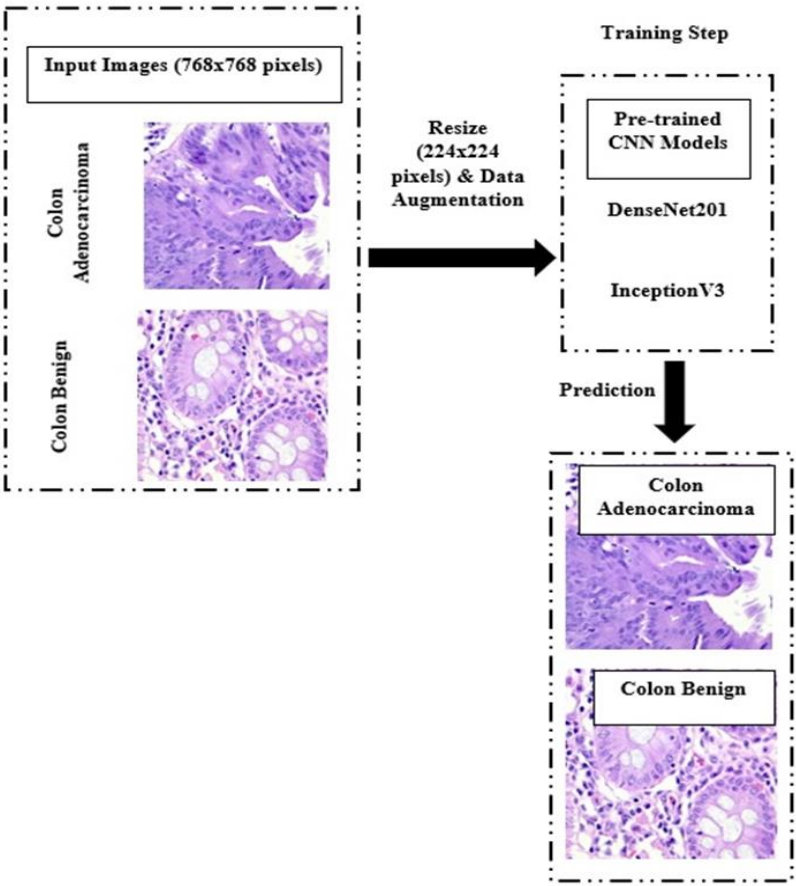

Figure 1: Block diagram of proposed deep neural network-based model

2.1 Colon cancer dataset

The dataset used in this study includes LC25000 lung and colon cancer histopathological images provided as open source in GitHub repository (Kaggle, 2023). This dataset contains 25000 images, of which 10000 belong to the type of colon cancer. Colon cancer dataset consisting of 5000 benign and 5000 adenocarcinoma

images is in jpeg format with 768x768 resolution. Histopathological images of colon cancer belonging to adenocarcinoma and benign classes are presented in Figure 2, respectively.

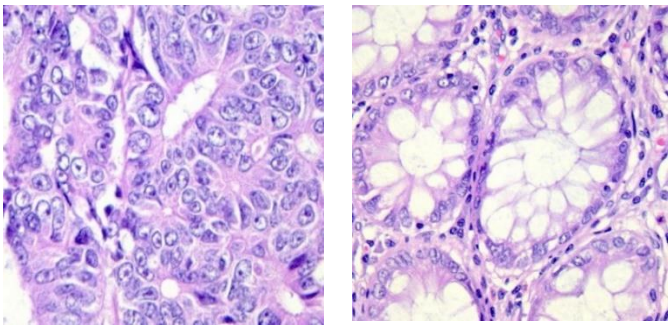

(a) *(b)*

Figure 2. Representative class samples of colon cancer histopathological image dataset (a) colon adenocarcinoma (b) colon benign

In this study, histopathological images of 1000 benign and 1000 adenocarcinomas in the colon cancer dataset are included. The original images (768 x 768 pixels) in the data set are resized to 224 x 224 pixels to be used within the scope of study. The parameters required for the data augmentation method in the training dataset are scaling factor = 1./255, shear range = 0.1, zoom range = 0.1, and horizontal flip.

2.2 Convolutional neural network model

Deep learning, a sub-branch of artificial intelligence, is one of the machine learning methods. The difference between deep learning and machine learning is the use of multilayer artificial

neural networks in deep learning. Thus, deep learning produces more successful results (Nasip & Zengin, 2018). In deep learning, the output is estimated depending on the data set used and the training of artificial intelligence is carried out depending on the result. Deep learning generally consists of an input layer, three or more hidden layers, and an output layer. The fact that deep learning includes more than one layer makes the learning process more successful. In the hidden layer, all complex operations that enable learning are carried out and learning algorithms are applied. In the input and output layers, no operation is performed. The biggest contribution of these layers in the field of artificial intelligence is that they can produce answers between 0 and 1 other than 0 and 1. Thus, more detailed solutions are obtained by dealing with a problem more specifically (Nasip & Zengin, 2018). Deep learning has recently been widely used in pattern recognition and image classification processes.

Convolutional Neural Network (CNN), which is widely used in image processing in deep learning, is based on the visual perception mechanism of living things. This algorithm is used in classification, clustering, object recognition, medical image analysis and natural language processing. CNN consists of convolution, pooling and fully connected layers. Deep features are obtained by applying filtering processing to the image in the convolution layer. In the pooling layer, which is usually used after each convolution layer, the size of the high-dimensional data set in the previous layers is reduced. This layer works according to the principle of taking the average (average pooling) of the neighboring elements in certain areas or taking the largest (max

pooling) of the neighboring elements. In the activation layer, the thresholding process is performed by passing the data through the selected activation function. The features obtained from the convolution and pooling layers are transferred to the fully connected layers for classification. This layer performs similar functions with traditional artificial neural networks (Uzen, Yeroglu & Hanbay, 2019).

In this study, a comparison of deep learning techniques with different models that can classify colon cancer images as colon adenocarcinoma and colon benign is made. In this direction, InceptionV3 and DenseNet201 deep learning techniques are used. The Inception network belonging to CNN includes InceptionV1, InceptionV2 and InceptionV3 versions of the Keras library. In this study, analyzes are carried out using the InceptionV3 model, which is developed in 2016 (Sezegedy et al., 2016). Based on InceptionV1, InceptionV3 has higher accuracy. In addition, compared to other models (InceptionV1 and InceptionV2), the number of parameters has been reduced and the training speed has been increased. InceptionV3 adjusts the depth and width of the network optimally to ensure the highest flow of information from the network (Bozkurt, 2021). DenseNet is one of the deep learning models used to classify the classes contained in datasets consisting of images. The DenseNet201 model, which is a new version of DenseNet model, are used in the study (Huang et al., 2017; El Gannour et al., 2021). The DenseNet201 model has the possibility to reuse features by different layers, which increases variation and performance in the next layer input. Therefore, it benefits from a

condensed network that is easy to train and can provide highly parametrically efficient models (Jaiswal et al., 2021).

2.3 Performance metrics

The performances of deep learning models created for the classification of colon cancer are compared regarding the criteria calculated using the confusion matrix. These metrics are accuracy, specificity, sensitivity, precision, and F1-Score. The mathematical formulas of these metrics can be expressed as follows:

$$Accuracy = \frac{TP+TN}{TP+TN+FP+FN} \quad (1)$$

$$Precision = \frac{TP}{TP+FP} \quad (2)$$

$$Sensitivity = \frac{TP}{TP+FN} \quad (3)$$

$$Specificity = \frac{TN}{TN+FP} \quad (4)$$

$$F1-Score = \frac{2*Precision*Sensitivity}{Precision+Sensitivity} \quad (5)$$

where TP is true positive, TN is true negative, FP is false positive, and FN is false negative.

3. Results and Discussion

In this study, experimental studies are carried out using Python programming language and Keras library in Google Colaboratory environment containing Tesla K80 Graphics Processing Unit (GPU). Two different pre-trained deep learning networks, InceptionV3 and DenseNet201 models, are employed to classify colon cancer. The categorical cross-entropy function with ADAM optimizer (β_1 = 0.9 and β_2 = 0.999) is used to pre-train

these models with random initialization weights. For each experiment, batch size (2, 3, 4, 8, 16 and 32), learning rate (1e-5), and number of epochs (30, 40 and 50) are all experimentally examined. The study's histopathological image dataset used is randomly divided into 80% training and 20% test.

Graphics of training/test accuracy and loss values for 30, 40, and 50 epochs of pre-trained DenseNet201 model are given in Figure 3, Figure 4, and Figure 5, respectively. 30, 40 and 50 epochs are run separately with different selected batch size values (2, 3, 4, 8, 16 and 32). When looking at Figure 3-5 in detail, it is clear that when batch size is set to 16 and 32 for 30, 40, and 50 epochs, the balance between train and test loss values offers more accurate results.

In our previous study (Kaya, Senyer Yapici & Uzun Arslan, 2022), batch size values used in InceptionV3 model, just as used in DenseNet201 model, were tested for 30 and 40 epochs. Overall classification accuracy was obtained as 100% (at batch size = 4, 8, 16 and 32), 99.75% (at batch size = 2 and 3) for 30 epochs and 100% (at batch size = 3, 8 and 32), 99.75% (at batch size = 4 and 16), 99.50% (at batch size = 2) for 40 epochs in InceptionV3 model (Kaya, Senyer Yapici & Uzun Arslan, 2022). In addition to that, in this study, InceptionV3 model is also performed for 50 epochs. Related graphics of training/test accuracy and loss values for 50 epochs of pre-trained InceptionV3 model are given in Figure 6. Similar to the results obtained in DenseNet201 model, the balance between the train and test loss values in InceptionV3 model for 50 epochs produces more accurate results at batch size = 16 and 32, as shown in Figure 6.

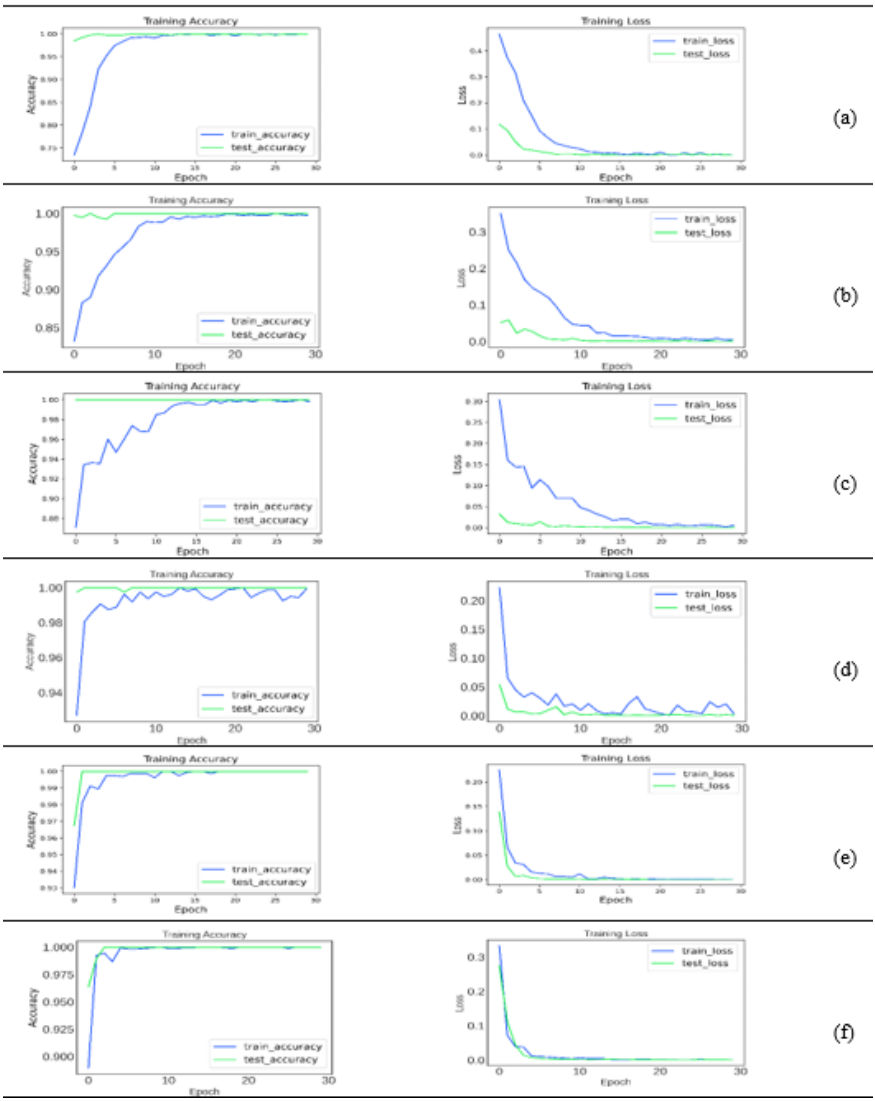

Figure 3: Training/test accuracy and loss values for 30 epochs in DenseNet201 where (a) batch size=2 (b) batch size=3 (c) batch size=4 (d) batch size=8 (e) batch size=16 (f) batch size=32

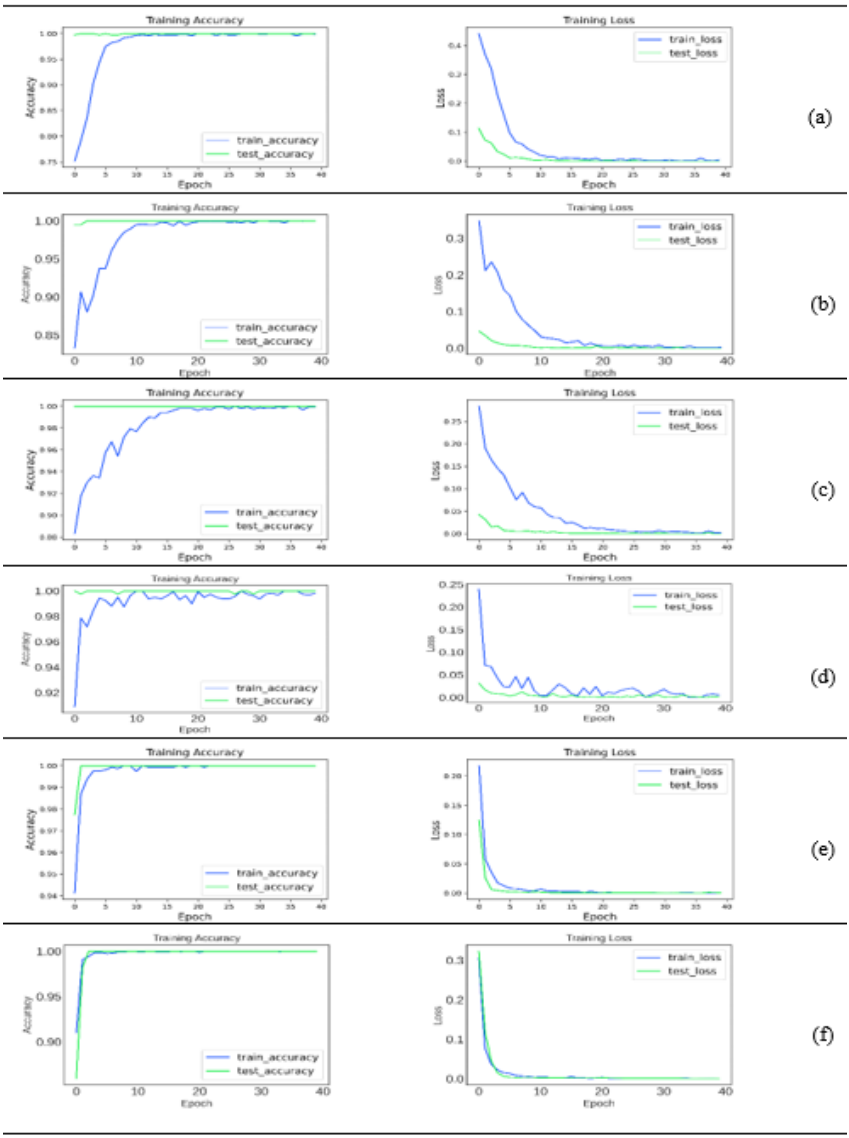

Figure 4: Training/test accuracy and loss values for 40 epochs in DenseNet201 where (a) batch size=2 (b) batch size=3 (c) batch size=4 (d) batch size=8 (e) batch size=16 (f) batch size=32

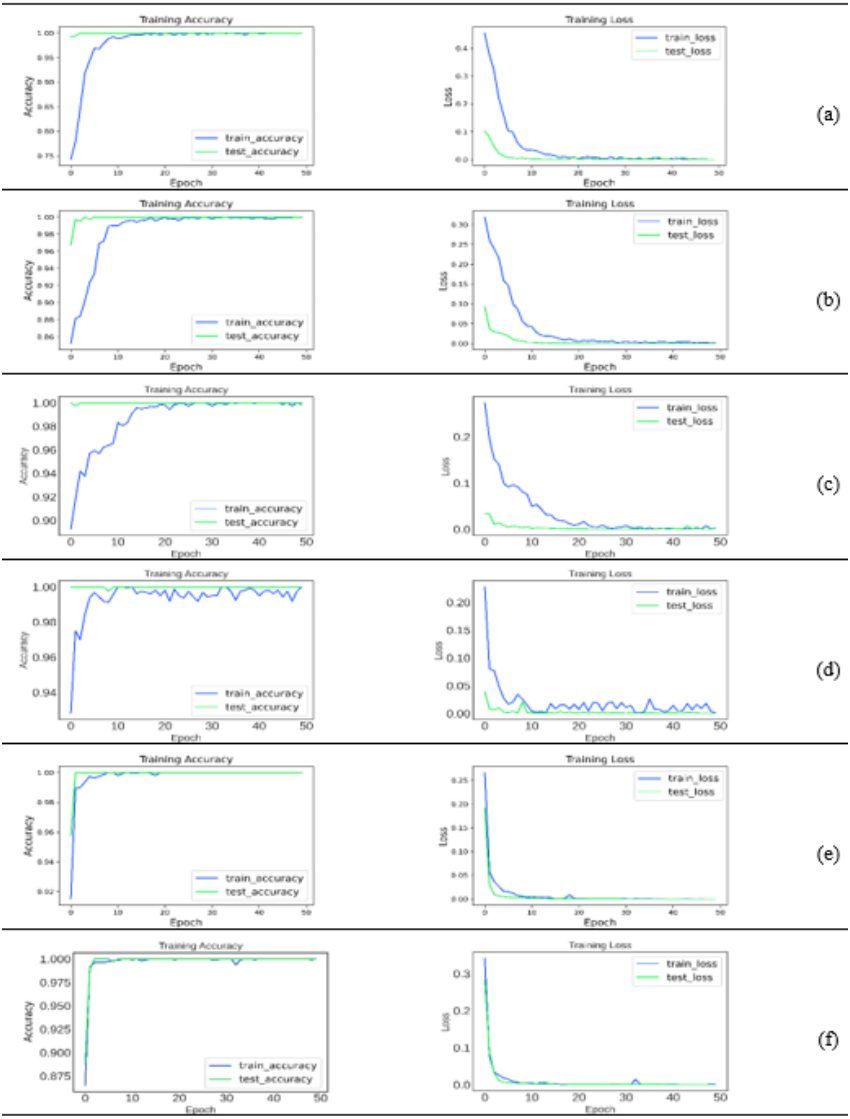

Figure 5: Training/test accuracy and loss values for 50 epochs in DenseNet201 where (a) batch size=2 (b) batch size=3 (c) batch size=4 (d) batch size=8 (e) batch size=16 (f) batch size=32

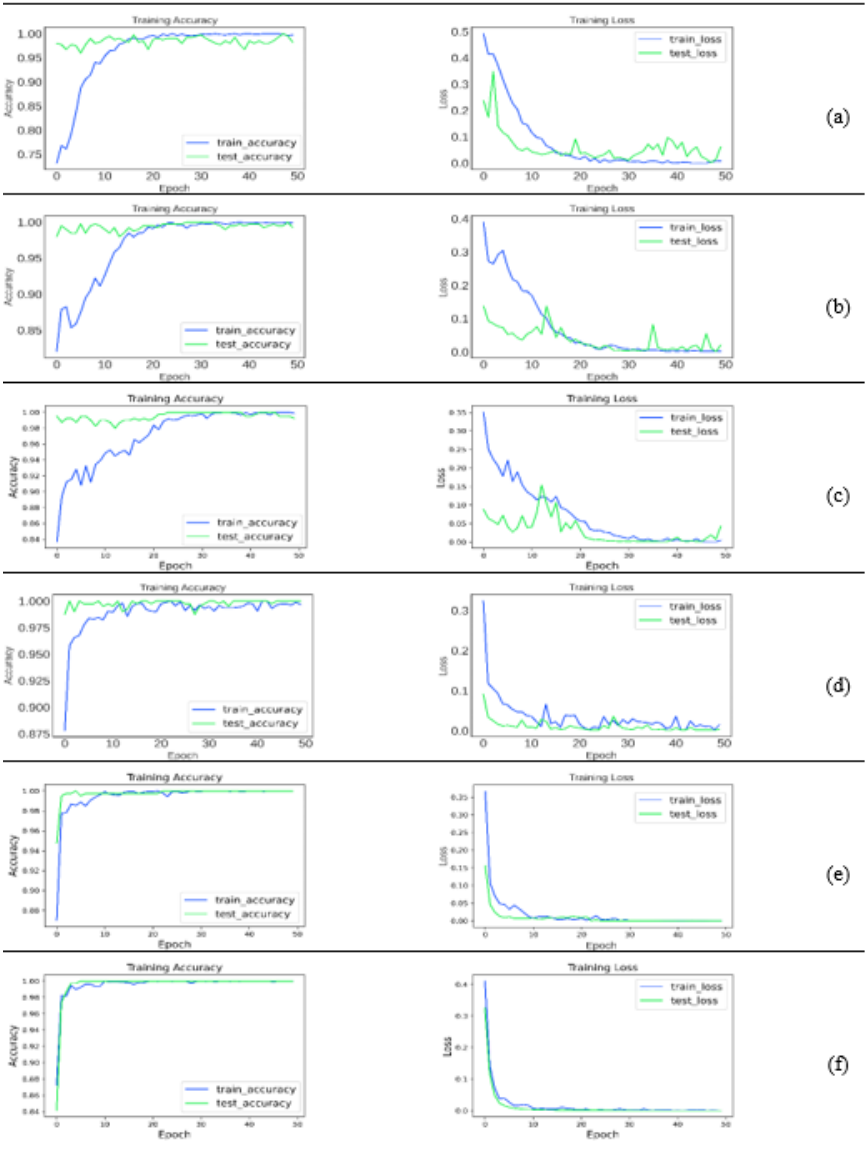

Figure 6: Training/test accuracy and loss values for 50 epochs in InceptionV3 where (a) batch size=2 (b) batch size=3 (c) batch size=4 (d) batch size=8 (e) batch size=16 (f) batch size=32

In Figure 7 and Figure 8, confusion matrices of colon adenocarcinoma and colon benign test results obtained from pre-trained InceptionV3 (for 50 epochs) and DenseNet201 models (for 30, 40 and 50 epochs) at different batch size values (2, 3, 4, 8, 16 and 32) are displayed, respectively. These confusion matrices are matched with experimental results from the graphics in Figures 3-6.

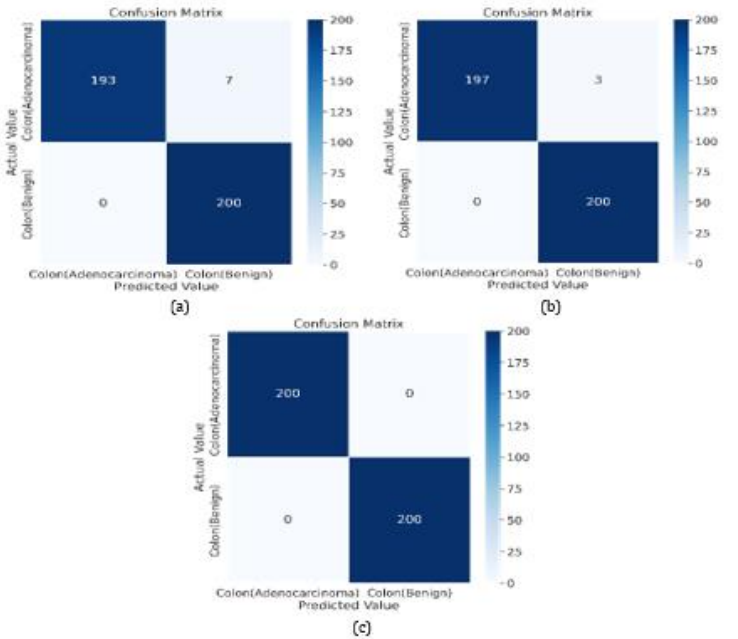

Figure 7: Confusion matrix for 50 epochs in InceptionV3 where (a) batch size=2 (b) batch size=3, 4 (c) batch size=8, 16, 32

Five performance metrics (accuracy (Acc.), specificity (Spec.), sensitivity (Sens.), precision (Prec.), and F1-Score) are calculated for pre-trained InceptionV3 and DenseNet201 models from related confusion matrices as seen above in Figure 7 and Figure 8. Classification performance results obtained from the models are presented in Table 1 and Table 2 in detail, respectively.

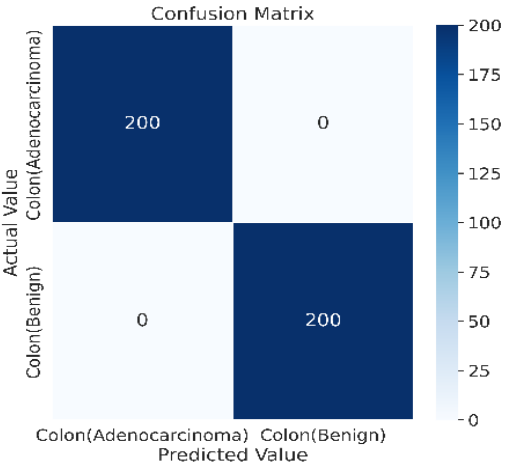

Figure 8: Confusion matrix for 30, 40 and 50 epochs in DenseNet201 (a) batch size=2, 3, 4, 8, 16, 32

Table 1: Evaluation metrics of pre-trained InceptionV3 model for different batch sizes

Epochs	Batch Size	Acc. (%)	Spec. (%)	Sens. (%)	Prec. (%)	F1-Score (%)
50	2	98.25	96.62	100	96.5	98.22
	3	99.25	98.52	100	98.5	99.24
	4	99.25	98.52	100	98.5	99.24
	8	100	100	100	100	100
	16	100	100	100	100	100
	32	100	100	100	100	100

Table 2: Evaluation metrics of pre-trained DenseNet201 model for different batch sizes

Epochs	Batch Size	Acc. (%)	Spec. (%)	Sens. (%)	Prec. (%)	F1-Score (%)
30-40-50	2	100	100	100	100	100
	3	100	100	100	100	100
	4	100	100	100	100	100
	8	100	100	100	100	100
	16	100	100	100	100	100
	32	100	100	100	100	100

As seen in Table 1, overall classification accuracy is obtained as 100% (at batch size = 8, 16 and 32), 99.25% (at batch size = 3 and 4), and 98.25% (at batch size = 2) in InceptionV3 model for 50 epochs. Similarly, Table 2 shows that for all epochs and batch sizes, overall classification accuracy, specificity, sensitivity, precision, and F1-Score are all 100%. When compared to pre-trained InceptionV3 model, pre-trained DenseNet201 model has a higher consistent classification accuracy. In addition to that, the classification performance of DenseNet201 model is also better than InceptionV3 model within 30 and 40 epochs, as seen in Table 2 and (Kaya, Senyer Yapici & Uzun Arslan, 2022).

4. Conclusion

Early detection of colon cancer, which is one of the most common types of cancer in the world, is critical for complete eradication of illness. In this study, we present two deep pre-trained DenseNet201 and InceptionV3 models for automatically predicting colon cancer using histopathological images acquired from colon benign and colon adenocarcinoma patients. The dataset contained 1600 histopathological colon cancer images is used to train the models and 400 images to test them. In the light of our findings, it is apparently observed that DenseNet201 model has higher and stable classification performance with 100% overall accuracy at batch size = 2, 3, 4, 8, 16 and 32 for 30, 40 and 50 epochs according to InceptionV3 model (99.75% accuracy at batch size = 2 and 3 for 30 epochs), (99.50% accuracy at batch size = 2, 99.75% accuracy at batch size = 4 and 16 for 40 epochs), and (98.25% accuracy at batch size = 2, 99.25% accuracy at batch size = 3 and 4 for 50 epochs). This research sheds light on how deep transfer

learning models can be used to detect colon cancer early on. The performance of different CNN models will be assessed in future investigations by increasing the amount of histopathological colon cancer images.

5. References

Abdelsamea, M. M., Pitiot, A., Grineviciute, R. B., Besusparis, J., Laurinavicius, A., & Ilyas, M. (2019). A cascade-learning approach for automated segmentation of tumour epithelium in colorectal cancer. *Expert Systems with Applications*, *118*, 539-552.

Bozkurt, F. (2021). Derin öğrenme tekniklerini kullanarak akciğer X-ray görüntülerinden Covid-19 tespiti. *Avrupa Bilim ve Teknoloji Dergisi*, (24), 149-156.

Bray, F., Ferlay, J., Soerjomataram, I., Siegel, R. L., Torre, L. A., & Jemal, A. (2018). Global cancer statistics 2018: GLOBOCAN estimates of incidence and mortality worldwide for 36 cancers in 185 countries. *CA: a cancer journal for clinicians*, *68*(6), 394-424.

El Gannour, O., Hamida, S., Cherradi, B., Al-Sarem, M., Raihani, A., Saeed, F., & Hadwan, M. (2021). Concatenation of pre-trained convolutional neural networks for enhanced COVID-19 screening using transfer learning technique. *Electronics*, *11*(1), 103.

Gessert, N., Bengs, M., Wittig, L., Drömann, D., Keck, T., Schlaefer, A., & Ellebrecht, D. B. (2019). Deep transfer learning methods for colon cancer classification in confocal laser microscopy images. *International journal of computer assisted radiology and surgery*, *14*, 1837-1845.

Graham, S., Chen, H., Gamper, J., Dou, Q., Heng, P. A., Snead, D., ... & Rajpoot, N. (2019). MILD-Net: Minimal

information loss dilated network for gland instance segmentation in colon histology images. *Medical image analysis*, *52*, 199-211.

Hatuwal, B. K., & Thapa, H. C. (2020). Lung cancer detection using convolutional neural network on histopathological images. *Int. J. Comput. Trends Technol*, *68*(10), 21-24.

Huang, G., Liu, Z., Van Der Maaten, L., & Weinberger, K. Q. (2017). Densely connected convolutional networks. In *Proceedings of the IEEE conference on computer vision and pattern recognition* (pp. 4700-4708).

Jaiswal, A., Gianchandani, N., Singh, D., Kumar, V., & Kaur, M. (2021). Classification of the COVID-19 infected patients using DenseNet201 based deep transfer learning. *Journal of Biomolecular Structure and Dynamics*, *39*(15), 5682-5689.

Kaggle (2023). *Lung and colon cancer histopathological images.* (Retrived from: https://www.kaggle.com/andrewmvd/lung-and-colon-cancer-histopathological-images, Accessed: 11.03.2024)

Kassani, S. H., Kassani, P. H., Wesolowski, M. J., Schneider, K. A., & Deters, R. (2022). Deep transfer learning based model for colorectal cancer histopathology segmentation: A comparative study of deep pre-trained models. *International Journal of Medical Informatics*, *159*, 104669.

Kaya, C., Senyer Yapici, I., & Uzun Arslan, R. (2022). Colon cancer outcome prediction from histopathological images using deep convolutional neural network. *4th International Engineering Research Symposium (INERS'22)*, 4-6 March 2022, Düzce, Türkiye, (pp. 287-294).

Masud, M., Sikder, N., Nahid, A. A., Bairagi, A. K., & AlZain, M. A. (2021). A machine learning approach to diagnosing lung and colon cancer using a deep learning-based classification framework. *Sensors*, *21*(3), 748.

Nasip, Ö. F., & Zengin, K. (2018, October). Deep learning based bacteria classification. In *2018 2nd international symposium on multidisciplinary studies and innovative technologies (ISMSIT)* (pp. 1-5). IEEE.

Nishio, M., Nishio, M., Jimbo, N., & Nakane, K. (2021). Homology-based image processing for automatic classification of histopathological images of lung tissue. Cancers, 13(6), 1192.

Pavlopoulou, A., Spandidos, D. A., & Michalopoulos, I. (2015). Human cancer databases. *Oncology reports*, *33*(1), 3-18.

Siegel, R. L., Miller, K. D., Goding Sauer, A., Fedewa, S. A., Butterly, L. F., Anderson, J. C., ... & Jemal, A. (2020). Colorectal cancer statistics, 2020. *CA: a cancer journal for clinicians*, *70*(3), 145-164.

Subramanian, P. G., Jain, A., Shivapuji, A. M., Sundaresan, N. R., Dasappa, S., & Rao, L. (2020). Plasma-activated water from a dielectric barrier discharge plasma source for the selective treatment of cancer cells. *Plasma Processes and Polymers*, *17*(8), 1900260.

Szegedy, C., Vanhoucke, V., Ioffe, S., Shlens, J., & Wojna, Z. (2016). Rethinking the inception architecture for computer vision. In Proceedings of the IEEE conference on computer vision and pattern recognition (pp. 2818-2826).

Teramoto, A., Tsukamoto, T., Kiriyama, Y., & Fujita, H. (2017). Automated classification of lung cancer types from cytological images using deep convolutional neural networks. *BioMed research international*, *2017*.

THSK (2017), *Türkiye Kanser İstatistikleri 2017*. (Retrived from: https://hsgm.saglik.gov.tr/tr/kanser-istatistikleri.html, Accessed: 11.03.2024).

Toğaçar, M. (2021). Disease type detection in lung and colon cancer images using the complement approach of inefficient sets. Computers in Biology and Medicine, 137, 104827.

Uçkuner, M., & Erol, H. (2021, September). A New Deep Learning Model for Skin Cancer Classification. In *2021 6th International Conference on Computer Science and Engineering (UBMK)* (pp. 27-31). IEEE.

Üzen, H., Yeroğlu, C., & Hanbay, D. (2019, September). Development of CNN architecture for Honey Bees disease condition. In *2019 International Artificial Intelligence and Data Processing Symposium (IDAP)* (pp. 1-5). IEEE.

Vuong, T. L. T., Lee, D., Kwak, J. T., & Kim, K. (2020, January). Multi-task deep learning for colon cancer grading. In *2020 International conference on electronics, information, and communication (ICEIC)* (pp. 1-2). IEEE.

Wang, S., Wang, T., Yang, L., Yang, D. M., Fujimoto, J., Yi, F., ... & Xiao, G. (2019). ConvPath: a software tool for lung adenocarcinoma digital pathological image analysis aided by a convolutional neural network. *EBioMedicine*, *50*, 103-110.

BÖLÜM V

The Relationship Between Renewable And Non-Renewable Electrical Energy Production And Consumption And Carbon Footprint

İnci BİLGE[1]
Emre AYDEMİR[2]

Introduction

The exponential growth of the global population leads to a surge in both the demand for and supply of electrical energy. Electrical energy production is provided from renewable sources as well as non-renewable sources. Figure 1 depicts wind turbines, solar panels, and thermal and hydroelectric power plants.

[1] Burdur Mehmet Akif Ersoy Üniversitesi, Elektrik ve Enerji Bölümü, Burdur/Türkiye, Orcid: 0000-0002-0194-2759, incibilge1@gmail.com

[2] 2 Akdeniz Üniversitesi, Ziraat Fakültesi, Zootekni Bölümü, Antalya/Türkiye, Orcid: 000-0002-2451-8248, aydemir1825@gmail.com

Figure 1. *Electrical energy production plants*

Electrical energy production is provided from renewable sources as well as non-renewable sources. Figure 1 depicts wind turbines, solar panels, and thermal and hydroelectric power plants. Thermal power plants running on natural gas, thermal power plants running on coal, thermal power plants running on fuel oil, and thermal power plants running on diesel fuel can be examples of non-renewable resources. Wind turbines, solar panels, hydroelectric power plants, geothermal energy, and biomass can produce electrical energy using renewable energy sources.

According to TEİAŞ data, the total amount of electrical energy produced in Turkey in 2022 is given in Grafic 1 (TEİAŞ (2022)).

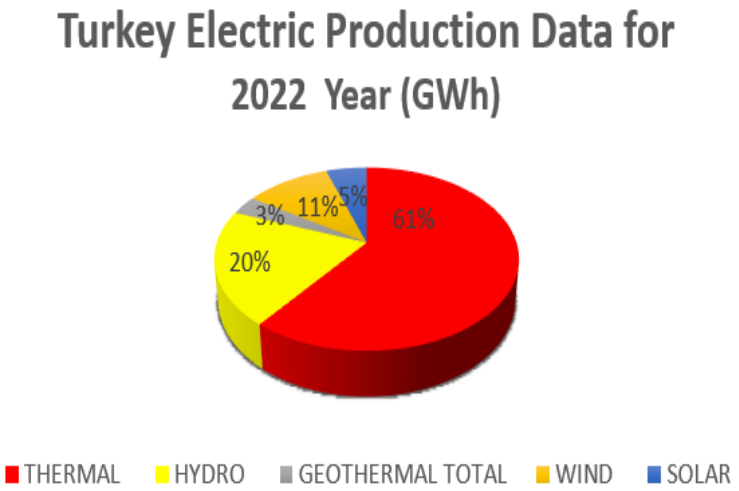

Graphic 1. *Electrical energy produced in Turkey in 2022*

Turkey Electricity Transmission Inc. Approximately 55.58 percent of Turkey's electricity production in May 2024 will come from renewable energy sources, with thermal power plants accounting for 47.17 percent. Solar energy contributes 9.92% to electricity production, wind turbines contribute 9.16%, hydroelectric power plants contribute 30.65%, geothermal energy contributes 3.1%, and biomass energy contributes 3% to the total generated electrical energy ("May 2024 Electricity Production," 2024).

According to these data, reducing fossil fuel use over time and increasing electrical energy production with renewable energy sources will have a positive impact on the carbon footprint. Graphic 2 shows the graph of TEİAŞ's electrical energy production data for May 2024.

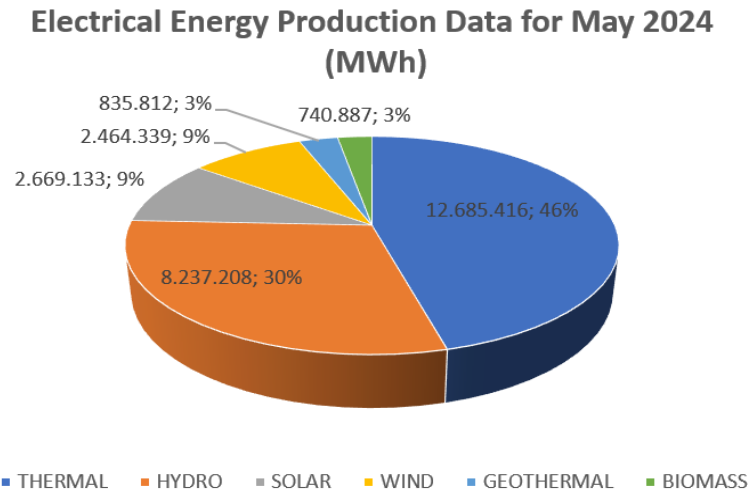

Graphic 2. *Electrical Energy Production Data for May 2024*

Carbon Footprint and Electricity Generation Methods

Carbon footprint is obtained from measuring the CO2 emissions that occur during the production, transportation, use and consumption stages of a product (Wiedmann and Minx, 2008). In this study, the energy sources used in electrical energy production are examined comparatively due to the carbon footprint formed during the production and consumption of electrical energy.

Variations in the techniques employed in the generation of electrical energy result in varying degrees of carbon emissions. Power plants that utilise fossil fuels like coal and natural gas emit a significant quantity of CO2, resulting in the largest carbon footprint among all other types of electrical energy production.

It is also stated that hydroelectric and nuclear power plants have lower carbon footprint values than thermal power plants because they do not cause CO2 emissions during electrical energy production (Wan-bin, 2012).

Furthermore, the utilisation of renewable energy sources such as wind, solar, and biomass for electricity production results in significantly reduced CO2 emissions compared to the use of fossil fuels, hence generating a minimal carbon footprint.

In a study conducted in South Africa regarding the effect of solar panels on carbon footprint, it is stated that solar energy production of electrical energy will be effective in increasing the country's economy as well as reducing greenhouse gas emissions and carbon footprint (Mutombo and Numbi, 2019).

Another study conducted in Australia concluded that the country's greenhouse gas emissions can be reduced by producing electrical energy using renewable energy sources (Wolfram et al., 2016).

Thermal power plants, which produce electrical energy using fossil fuels, constitute a significant part of the carbon footprint. Carbon emissions can be significantly reduced by adding carbon capture and storage technologies during electricity production in thermal power plants that run on coal, one of the fossil fuels. This technique has the potential to decrease greenhouse gas emissions and enhance the sustainability of electricity production (Saboori and Hemmati, 2016).

Relationship between solar energy and carbon footprint

Photovoltaic (PV) panels that produce electricity are sustainable because they do not cause CO2 emissions and prevent the greenhouse gas effect. In addition, unlike fossil fuels, solar energy does not produce carbon emissions as a result of electrical energy production, so it has a significant impact on reducing the carbon footprint. Therefore, increasing electricity production by using renewable energy sources instead of fossil fuels is extremely important in reducing the carbon footprint.

De Souza Grilo et al. (2018), in the literature on electrical energy production using PV panels, it was stated that the use of PV panels makes a significant contribution to reducing the carbon footprint. Expanding the utilisation of renewable energy sources not only diminishes carbon emissions but also offers a pristine energy source that avoids environmental damage (Sharif et al., 2019).

A study conducted in 30 provinces in China found that the carbon footprint was diminished as a result of the electricity generated by solar power plants (Zhao and Li, 2023).

Utilising photovoltaic (PV) panels for electricity generation promotes the enhancement of environmental sustainability (Dominguez-Ramos & Irabien, 2019).

A separate study conducted by Ito in 2017 discovered that the utilisation of renewable energy sources had a dual effect of decreasing carbon emissions and promoting economic growth in 42 developed countries.

The study analysed data from the years 2002 to 2011.Thermal power plants, which generate electricity by burning fossil fuels, make up a substantial portion of the carbon footprint. Carbon emissions can be substantially decreased by using carbon capture and storage technology in coal-fired thermal power plants, which are powered by one of the fossil fuels. The utilisation of this technology has the capability to reduce release of greenhouse gases and improve long-term viability of power generation (Saboori and Hemmati, 2016).

A recent study in the literature shown the efficacy of renewable energy power plants in mitigating carbon emissions (Kerem, 2022). Furthermore, a separate study advocated for the augmentation of renewable energy sources to mitigate the carbon

emissions associated with electricity generation (Alderson et al., 2012). Differences in the energy sources used in electrical energy production and their geographical distribution significantly affect the carbon footprint.

The Relationship Between Electricity Production and Carbon Footprint in Wind Turbines

Wind energy is one of the renewable energy sources and has an important role in reducing the carbon footprint by reducing the use of fossil fuels in electricity production. There are environmental factors that affect the efficiency of electrical energy produced by wind turbines.

Wind turbines electrical energy production is influenced by environmental conditions including wind speed, temperature, humidity, pressure, and precipitation. By enlarging the wind turbine, the efficiency of the generated electrical energy can be enhanced. The performance of wind farms is contingent upon fluctuations in temperature and wind velocity at the specific location of installation.
Regions with high wind speeds generate less electrical energy compared to regions with low wind speeds. Consequently, installing wind turbines in areas with low wind speeds may diminish the effectiveness of generating electrical energy. Furthermore, failure to choose suitable locations may result in decreased turbine efficiency (Haskew et al., 2016).

It is stated that since the production of electrical energy with wind energy does not cause greenhouse gas emissions, it can be effective in reducing global warming by significantly reducing the carbon footprint compared to fossil fuels (Mendecka and Lombardi, 2019).

The relationship between biomass electrical energy production and the carbon footprint

Burning fuels made of organic, biological, or plant materials produces electrical energy, and in addition to serving as an alternative to fossil fuels, biomass can lessen the greenhouse gas effect and carbon footprint (Adams and McManus, 2014).

Carbon footprint analysis in thermal power plants

Numerous studies in the literature examine the impact of electrical energy generated in thermal power plants on carbon footprint. These studies indicate that since thermal power plants create greenhouse gas emissions, these emissions should be reduced. Turkey Electricity Transmission Inc. According to (TEİAŞ) data, 38% of the electrical energy produced by Turkey in thermal power plants in May 2024 is provided by imported coal, 30% is provided by natural gas, 28% is provided by lignite coal and 3% is provided by hard coal while 1% was provided by fuel oil ("May 2024 Electricity Production," 2024). Graphic 3 shows the graph of Energy Produced in Thermal Power Plants in May 2024 (MWh).

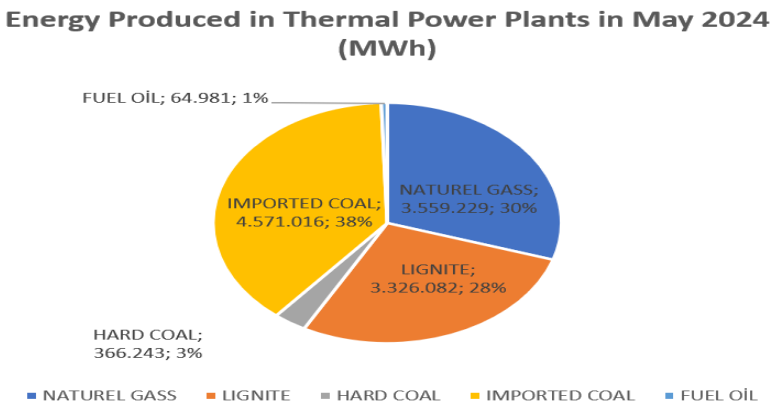

Graphic 3. *Energy Produced in Thermal Power Plants in May 2024 (MWh)*

As a result of the carbon footprint analysis of a thermal power plant located in Liaoning province of China, the total carbon footprint of the power plant is approximately 6.52 million tons, 90.23% of which is due to fuel combustion.

Lou et al. (2013) assert that carbon emissions can be diminished by enhancing energy efficiency and technological advancements. Electrofilters are capable of filtering a range of gases, including carbon dioxide, which is released during the combustion of fossil fuels in thermal power plants, with the aim of diminishing the carbon footprint.

Oxy-fuel combustion power cycles are a technique used in the energy sector to reduce carbon dioxide emissions. Compared to the combined cycle with carbon dioxide capture, the Allam cycle is more efficient and has lower carbon dioxide emissions as well as lower installation costs. (Rogalev et al.,2021). Utilising the waste heat produced in thermal power plants for residential heating purposes leads to a decrease in carbon emissions, as well as a reduction in the consumption of natural gas and coal for residential heating.

It is of critical importance as it will reduce the carbon footprint by increasing energy efficiency in thermal power plants. According to Prisyazhniuk (2008), fuel consumption and carbon emissions can be decreased by improving energy efficiency through the use of advanced technologies like magneto-hydrodynamic resonance and the Kalina cycle.

It is necessary to decrease global fossil fuel use due to the higher carbon emissions associated with thermal power plants that

utilise fossil fuels like coal, oil, and natural gas, compared to hydroelectric and nuclear power plants (Wan-bin, 2012).

Conclusion

Generating electrical energy from solar energy using solar panels is an important method to reduce the carbon footprint. Similar to solar energy, wind energy is a sustainable energy source that does not generate carbon emissions. Enhancing the electrical energy generation in wind turbines will effectively decrease the carbon footprint. Electrical energy produced in wind turbines varies depending on the selection of appropriate locations for wind turbines, the design of wind turbines, and environmental variables. These variables significantly affect the efficiency of the electrical energy produced by wind turbines.

Utilising wind energy through wind turbines for electricity production is an effective strategy to reduce carbon emissions, as it does not generate greenhouse gases, unlike the usage of fossil fuels. The burning of coal, a fossil fuel commonly utilised in thermal power plants, results in the emission of carbon dioxide (CO2) gas, consequently resulting in an increase in the carbon footprint. Carbon filters are essential for mitigating the carbon emissions produced by thermal power plants. Increasing energy efficiency in power plants where electrical energy is produced, using advanced technologies, and reducing dependence on fossil fuels will increase environmental sustainability and reduce carbon emissions. Expanding the use of renewable energy sources for electricity generation will not only increase environmental sustainability but also improve the economy and reduce carbon emissions.

Kaynaklar

Enerji Ajansı, (2024). URL https://enerjiajansi.com.tr/2024-mayis-ayi-elektrik-uretimi/ (accessed 21/06/24).

Adams, P.W.R., McManus, M.C., (2014). Small-scale biomass gasification CHP utilisation in industry: Energy and environmental evaluation. Sustainable Energy Technologies and Assessments 6, 129–140. https://doi.org/10.1016/j.seta.2014.02.002

Alderson, H., Cranston, G.R., Hammond, G.P., (2012). Carbon and environmental footprinting of low carbon UK electricity futures to 2050. Energy, 6th Dubrovnik Conference on Sustainable Development of Energy Water and Environmental Systems, SDEWES 2011 48, 96–107. https://doi.org/10.1016/j.energy.2012.04.011

Caduff, M., Huijbregts, M.A.J., Althaus, H.-J., Koehler, A., Hellweg, S., (2012). Wind Power Electricity: The Bigger the Turbine, The Greener the Electricity? Environ. Sci. Technol. 46, 4725–4733. https://doi.org/10.1021/es204108n

de Souza Grilo, M.M., Fortes, A.F.C., de Souza, R.P.G., Silva, J.A.M., Carvalho, M., (2018). Carbon footprints for the supply of electricity to a heat pump: Solar energy vs. electric grid. Journal of Renewable and Sustainable Energy 10, 023701. https://doi.org/10.1063/1.4997306

Haskew, B., Minogue, L., Woodley, R., Phaktham, A., Randunu, S., (2016). Environmental Effect on Wind Farm Efficiency and Power Production. PAM Review Energy Science & Technology 3, 137–152. https://doi.org/10.5130/pamr.v3i0.1412

Ito, K., (2017). CO2 emissions, renewable and non-renewable energy consumption, and economic growth: Evidence from panel data for developing countries. International Economics 151, 1–6. https://doi.org/10.1016/j.inteco.2017.02.001

Kerem, A., (2022). Investigation of carbon footprint effect of renewable power plants regarding energy production: A case study of a city in Turkey. Journal of the Air & Waste Management Association 72, 294–307. https://doi.org/10.1080/10962247.2022.2028690

Lou, L.L., Mu, H.L., Chen, X., Li, H.N., (2013). The Carbon Footprint Analysis of Thermal Power Plants. Advanced Materials Research 807–809, 814–821. https://doi.org/10.4028/www.scientific.net/AMR.807-809.814

Mendecka, B., Lombardi, L., (2019). Life cycle environmental impacts of wind energy technologies: A review of simplified models and harmonization of the results. Renewable and Sustainable Energy Reviews 111, 462–480. https://doi.org/10.1016/j.rser.2019.05.019

Mutombo, N.M.-A., Numbi, B.P., (2019). Assessment of renewable energy potential in Kwazulu-Natal province, South Africa. Energy Reports 5, 874–881. https://doi.org/10.1016/j.egyr.2019.07.003

Prisyazhniuk, V.A., (2008). Alternative trends in development of thermal power plants. Applied Thermal Engineering 28, 190–194. https://doi.org/10.1016/j.applthermaleng.2007.03.025

Rogalev, A., Rogalev, N., Kindra, V., Komarov, I., & Zlyvko, O. (2021). Research and Development of the Oxy-Fuel Combustion Power Cycles with CO2 Recirculation. *Energies*, *14*(10), Article 10. https://doi.org/10.3390/en14102927

Saboori, H., Hemmati, R., (2016). Considering Carbon Capture and Storage in Electricity Generation Expansion Planning. IEEE Transactions on Sustainable Energy 7, 1371–1378. https://doi.org/10.1109/TSTE.2016.2547911

Sharif, A., Raza, S.A., Ozturk, I., Afshan, S., (2019). The dynamic relationship of renewable and nonrenewable energy consumption with carbon emission: A global study with the application of heterogeneous panel estimations. Renewable Energy 133, 685–691. https://doi.org/10.1016/j.renene.2018.10.052

TEİAŞ (2022), TURKİYE-ELEKTRİK-URETİM-İLETİM-İSTATİSTİKLERİ URL https://www.teias.gov.tr/turkiye-elektrik-uretim-iletim-istatistikleri, (accessed 23/06/2024).

Wan-bin, S., (2012). Carbon footprint of global electricity and its equivalent calculation. Chinese Journal of Ecology.

Wiedmann, T., Minx, J., (2008). A Definition of ‘ Carbon Footprint’ ISA UK Research Report 0701.

Wolfram, P., Wiedmann, T., Diesendorf, M., (2016). Carbon footprint scenarios for renewable electricity in Australia. Journal of Cleaner Production 124, 236–245. https://doi.org/10.1016/j.jclepro.2016.02.080

Zhao, H., Li, Y., (2023). Impact of solar energy generation on carbon footprint: Evidence from China. Geological Journal 58, 3476–3486. https://doi.org/10.1002/gj.4827

BÖLÜM VI

Determination of Chick Quality Via Image Processing

Emre Aydemir
İnci Bilge

Introduction

With the increasing popularity around the world, the need for nutrients also increases. Inasmuch as this increasing need for nutrients and the limited production of various nutrients, the desired demand is not met. Especially; The fact that protein-based products do not meet the desired supply and are more expensive than other nutrients further increases the value of protein-based products. But; Among the protein-based products, poultry products are the most accessible protein-based product due to both their high protein content and affordable price performance. With the increasing need for food, the amount of production increases significantly throughout the world. However, with this increasing

amount of production, one of the problems encountered during production in the sector is chick quality. Chick quality is one of the main criteria affecting the profitability of production (Stardig et al. 2016). In this way, as chick quality increases, production profitability also increases.

To increase this profitability, qualitative and quantitative methods are used to determine chick quality. Especially with the developing technology, these methods have begun to be replaced by advanced technologies such as artificial intelligence (Asadi and Raoufat 2010).

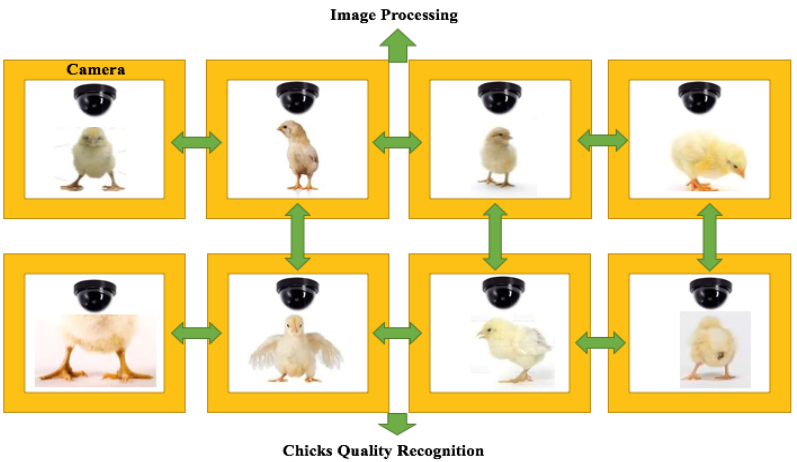

Especially in recent years, image processing methods used to determine egg and meat quality have attracted attention. One of the biggest aids in determining chick quality by image processing method is the number of pixels (Asadi and Raoufat 2010). Moreover; The number of digital images formed may vary depending on the number of pixels, pixel width, optical filter, number and quality of optical lenses. Depending on this, chick quality is affected positively or negatively.

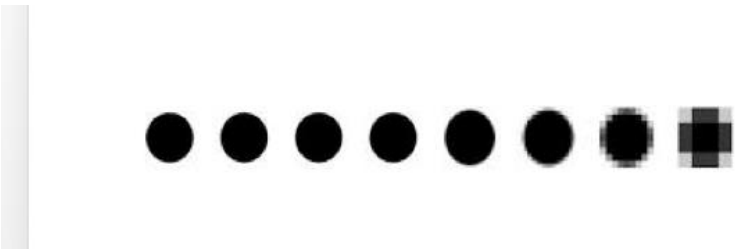

In addition, various algorithms and mathematical models are used to classify chick quality. For example; thanks to morphometric measurements, chick quality may be determined within the total area in pixels (Tao et al. 2004). In other words, based on image processing algorithms; helps determine chick quality by using morphometric variables created by the average length of the total area in pixels along with the data obtained and the developed technique.

Chick quality

Qualitative and quantitative methods are used to determine the physical characteristics of the chick. These methods are determined by using morphological measurements such as chick viability, developmental status, chick weight, leg length, chest area, bone development, body posture, leg structure, belly closure,

deformities in the beak, eyes and legs, and shank diameter (Molenaar 2018).

Image processing

Images taken from the model chick; It is processed in a computer environment (Gonzalez and Woods, 2005). First, the preliminary preparation phase of the image is by removing the image blur on it; the image is sharpened. Moreover; The captured image can be subjected to low, medium, and high-level processing.

The processing of the image taken from the chick during the entry and exit processes is low-level. Segmentation and description processes during the recognition and classification of objects in the received image are intermediate-level operations. Recognizing the objects in the images and analyzing the images are high-level processes.

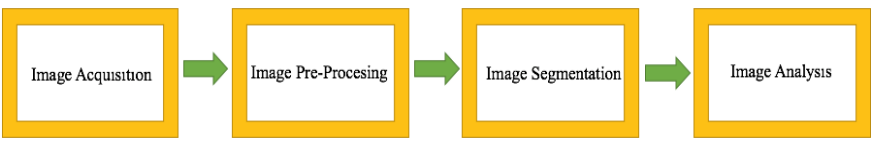

By analyzing the image taken from the model chick in a computer environment; It is the detailed determination of the image content of the objects found in the images (Jähne, 2005). In this way, the model ensures the accuracy of the score in determining the quality of the chick.

Image pre- processing

Pre-processing of the image received from the model chick, filtering, graying the image, and converting it into a binary image are performed on the received image, respectively. In this application, it helps to make the image more distinct and easily processed (Palchikova et al. 2018; Seo et al. 2019; Ma et al. 2022).

Digital imaging

To create a digital image of the image taken from the model chick, the energy emitted electromagnetically from the analog image can be establish and converted into a digital signal. In addition, the digital image is created by sampling the 2-dimensional image function existing in real life using the sampling technique (Palchikova et al. 2018; Seo et al. 2019; Li et al. 2020).

Color image processing

The model appears in image processing analysis, such as description and extraction of the image taken from the chick. Its visibility electromagnetic spectrum ranges between approximately 400 nm and 700 nm. This helps determine the quality score of the model creature by determining visible colors (Norouzi et al. 2014; Ma et al. 2022; Han et al. 2018).

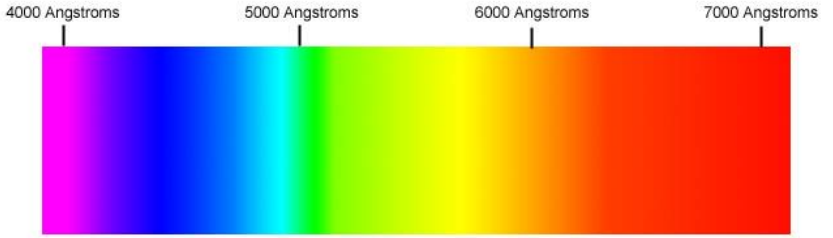

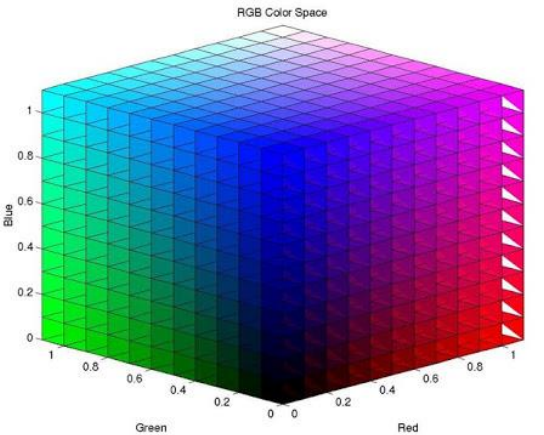

Image processing and histograms

The histogram of the image from the model chick is a plot of the number of image pixels against a specific brightness value. By adjusting the brightness value of each pixel of the model chick's image, corrections in image brightness and contrast are achieved (Seo et al. 2019; Li et al. 2020).

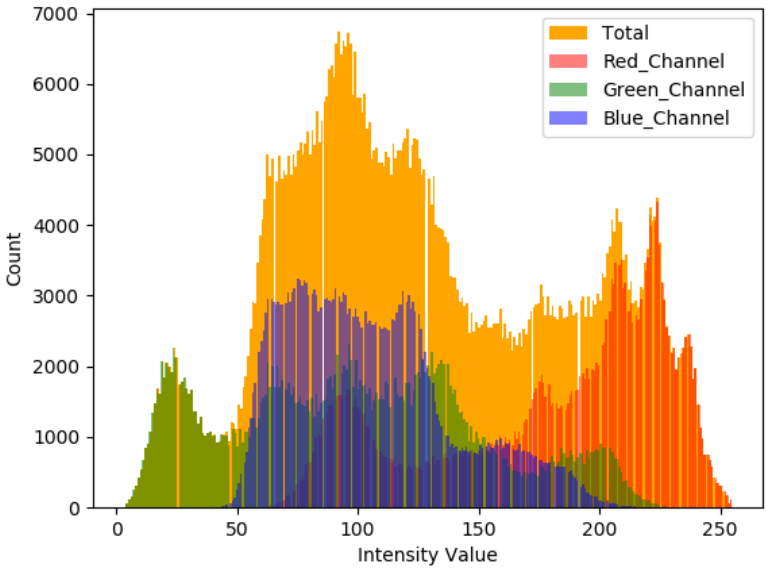

Color histogram

Color histogram of the image in determining chick quality; It refers to the color distribution in the image. The image taken from the model chick; The color histogram for a digital image is an indication of the number of pixels that have colors in each of the fixed list of the color space. Moreover; the color histogram of the image of the model chick is statistical and can be considered as a continuous distribution approximation (Palchikova et al. 2018; Li et al. 2020).

Histogram equalization

Using the histogram of images taken from the model chick; It is an image processing technique based on contrast adjustment; It provides a wide range of contrast enhancements for many images.

Also effective by emitting the most frequent brightness values; It helps in images with bright or dark backgrounds and foreground (Seo et al. 2019; Palchikova et al. 2018).

Image Segmentation

Dividing the digital image taken from the model into multiple compartments is called image clouding. In this way, it facilitates the analysis and expression of the image. It is also used to find objects and boundaries, lines, curves) in the image (Yan et al. 2020; Pare et al. 2020).

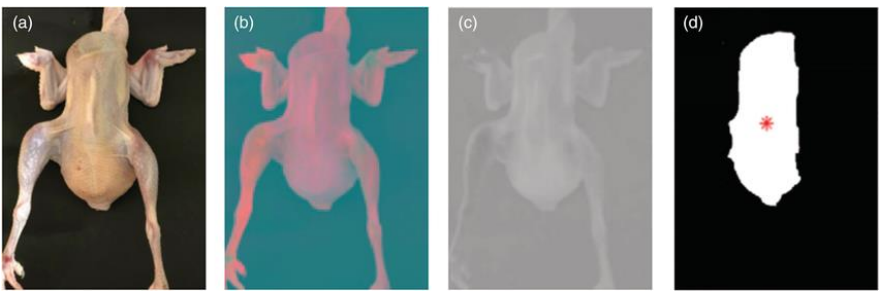

References

Asadi, V. And Raoufat, M. H. (2010). Egg weight estimation by machine vision and neural network techniques (a case study fresh egg). *International Journal of Engineering, Technology and Natural Sciences*, (2), 1-4.

Gonzalez R. C., Woods R. E. (2007). Digital Image Processing, 3Ed., (pp. 1-7), A.B.D., New Jersey : Prentice Hall.

Han, D., Sun, D., Zhang, L.: Linear rate convergence of the alternating direction method of multipliers for convex composite programming. Math. Oper. Res. 43(2), 622–637 (2018

Jähne, B. (2005). Digital Image Processing, Springer, 6Ed., (pp. 7-19), Berlin, 2005.

Li, Y., Cao, G., & Wang, T. (2020). A novel local region-based active contour model for image segmentation using Bayes theorem. *Information Sciences*, 506, 443–456.

Ma, G., Yan, Z., Li, Z., Zhao, Z.: Efficient Iterative Regularization Method for Total Variation-Based Image Restoration. Electronics 11(2), 258 (2022)

Molenaar, R., Reijrink, I., Meijerhof, R. and Van Den Brand, H. 2010. Meeting embryonic requirements of broilers throughout incubation; A Review. Revista Brasileira De Ciência Avícola;12(3):137-148.

Norouzi, A., Rahim, M.S.M., Altameem, A., Saba, T., Rad, A.E., Rehman, A., Uddin, M.: Medical image segmentation methods, algorithms, and applications. IETE Tech. Rev. 31(3), 199–213 (2014)

Tao, Y., Chen, Z., & Griffis, C. L. (2004). Chick feather pattern recognition. *IEE Proceedings - Vision, Image, and Signal Processing*, *151*(5), 337.

Palchikova, I. G., Smirnov, E. S., & Palchikov, E. I. (2018). Quantization noise as a determinant for color thresholds in machine vision. *Journal of the Optical Society of Americaa-Optics Image Science and Vision*, 35, 214–222.

Pare, S., Kumar, A., & Singh, G. K. (2020). Image segmentation using multilevel thresholding: A research review. *Iranian Journal of Science and Technology-Transactions of Electrical Engineering*, 44, 1–29.

Seo, Y., Lee, H., Mo, C., Moon, S., Baek, I., Lee, J., & Cho, B. (2019). Multispectral fluorescence imaging technique for on-line inspection of fecal residues on poultry carcasses. *Sensors*, 19(16), 2–16.

Stadig, L. M., Rodenburg, T. B., Reubens, B., Aerts, J., Duquenne, B., & Tuyttens, F. A. M. M. (2016). Effects of free-range access on production parameters and meat quality, composition and taste in slow-growing broiler chickens. *Poultry science*, *95*(12), 2971-2978. https://doi.org/10.3382/ps/pew226

Yan Chen, Hui Ai and Shuo Li, 2020, Analyis of correlation Between carcass and viscera for chicken eviscerating based on machine vision technology, Journal of Food Process Engineering, 25.

BÖLÜM VII

Determination of Scattering Parameters in Horn Antenna Design Using Machine Learning Algorithm

Ahmet Arif ULUSLU[1]
Gülsüm ARI[2]

Introductıon

With the development of wireless communication systems, the need for compact, efficient and high-performance antenna design has increased. Antennas, which are an important part of wireless communication systems, must have certain performance evaluation levels such as gain, radiation diagram, operating band and return loss (Tirkas & Balanis, n.d.). Antennas are generally described in two ways, based on their size. Planar antennas such as patch antennas (Chen et al., 2023; Fang et al., 2022) or complex 3D

[1] Associate Prof. Dr, İstanbul University-Cerrahpaşa
[2] Lecturer, İstanbul University-Cerrahpaşa

antennas such as 2D and Horn antennas (Lee et al., 2023; Ren et al., 2021; Trzebiatowski et al., 2022; Wu et al., 2020). Antennas in the specified structures have advantages and disadvantages in terms of performance evaluations. Microstrip antennas require less design area and volume, so their production cost is low (Tirkas & Balanis, n.d.). However, it has limited bandwidth and low gain values that can only be improved by array design. Horn antennas require more design volume than microstrip antennas. However, Horn antennas are better in terms of bandwidth, gain values and radiation characteristics (Yan et al., 2021). Horn antenna is preferred in many applications requiring high-performance radiation diagram features and ultra-wideband operating range (Coburn & McCormick, 2018). Antenna design takes scattering parameters into account. Inefficiency at the antenna input significantly reduces the gain and therefore the radiation performance of the antenna, especially in ultra-wideband antennas. However, in ultra-wideband antenna designs, only scattering parameters are required. A design that has the desired scattering parameters may not have the expected radiation performance. Thus, the radiation performance of the design can be evaluated independently of the scattering parameter. Besides these features, other factors such as design size and volume must be taken into account, which limit the potential uses to which the antenna design can be put and directly affect production costs (Bongard et al., 2020; Jie et al., 2017; Jin et al., 2018; Montalvo et al., 2015). As a result, the design of a horn antenna that provides the desired performance criteria is a challenging and complex problem. To meet these requirements, an accurate electromagnetic (EM) characterization is necessary. For

this, design tools capable of performing full-wave electromagnetic analysis (TEM) are required. Although EM simulations provide high-precision measurements, they are at a disadvantage in solving computationally important and complex problems such as tolerance analyzes and optimization. The machine learning method is an effective solution method to eliminate the disadvantages of full-wave EM modeling, which is computationally inefficient and expensive. It has been proven to be used as a low-cost method in the design procedure of high-frequency devices. This can be used to calculate steps such as scattering parameters (I. Khan et al., 2018; Mahouti et al., 2022), reflection phase of reflective array antennas (T. Khan & De, 2012), characteristic impedance (Angiulli, 2009), and resonance frequency estimation of antenna designs (Valagiannopoulos & Tsitsas, 2008).

MATERIAL and METHOD

Dataset

The data set used in the machine learning model consists of 18750 data. These data consist of attributes used in the horn antenna design and forming the performance value of the design. It consists of 8 attributes and 1 label column. The attributes are radius, cone height, Aperture Radius, Waveguide Height, feed height, feed Width, feed offset and frequency value, respectively. The label value is created by the scattering parameter called S11. 2.2. Machine Learning and XGBoost Model Machine Learning method is an artificial intelligence method that offers the opportunity to work with many types of data simultaneously, especially numerical and categorical data. All data used in this study are features that determine the performance of horn antenna

data and all consist of numerical values. At the same time, the artificial intelligence model created is a regression model, that is, it can produce a numerical output from the values given to it, considering the task required of it. After determining the desired task from the model, the next stage is to determine the model algorithm that will perform and the hyperparameters of this model. The machine learning model used in this study is the XGBoost algorithm, which is a gradient-based learning algorithm. It works with the logic of decision trees based on the XGBoost algorithm and uses an ensemble learning method. Gradient-based learning algorithms use bagging and boosting methods due to their structure. These two learning pairs extract samples with k elements in the dataset consisting of N_samples data and introduces them to individual trees, thus forming a collective tree learning model. In other words, the XGBoost model is a machine learning algorithm where a collection of weak tutors combine to form a strong final learning model. The machine learning method is based on statistical information rather than deep learning, which is another popular intelligence method. The error metrics to be used when examining the performance of the models established in this method are determined according to these statistical methods. The performance metrics used in this study are Mean Squared Error (MSE), Root Mean Squared Error (RMSE) and R^2, respectively. To explain briefly, MSE is a measure of the average squared difference between the predicted values and the actual values. The mathematical formula is:

$$MSE = \frac{1}{n}\sum_{i=1}^{n}(y_i - \hat{y}_i)^2 \quad (1)$$

Another performance metric is RMSE. RMSE is the square root of MSE. It provides an estimate of the standard deviation of the prediction errors. If expressed with a mathematical formula, RMSE is:

$$RMSE = \sqrt{MSE} = \sqrt{\frac{1}{n}\sum_{i=1}^{n}(y_i - \hat{y}_i)^2}$$

(2)

And the last performance metric, R2, takes a value between 0 and 1, indicating how close the predictions made by the regression model are to the real predictions. During modeling, 30% of 18750 pieces of data were separated into training and testing. As a result, 13125 training and 5625 testing data were obtained. XGBoost learned the model with the data allocated for training and evaluated itself with the data allocated for testing. While creating the model architecture, the GridSearchCV method was used without determining the hyperparameter values. Thus, the most appropriate hyperparameter values for the model and dataset were obtained. In addition, with the "n_estimator" parameter, which determines the number of trees in the community, one of these hyperparameters, the change in the performance metric of the model with each tree added to the model can be examined. The specified graphics are below

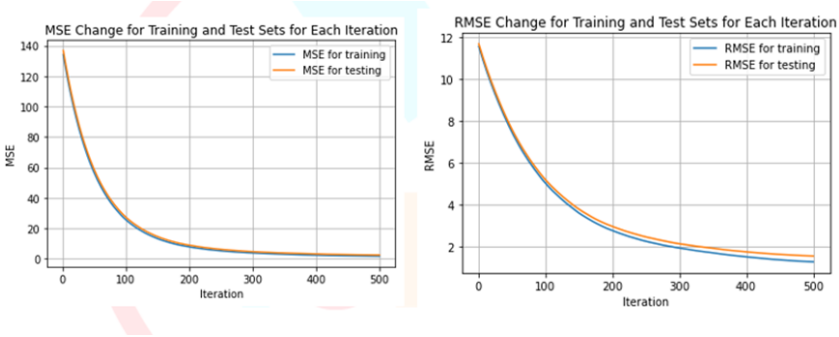

Figure 6:Variation of performance metrics in each tree

While the model is in the learning phase in the data set, it tries to train itself by establishing relationships between the attributes. In the XGboost model, which performs treetype learning, the algorithm establishes more relationships between some attributes, that is, it encounters those attributes more often. These attributes are called high-weight labels. Even though he encounters some of them less frequently, he achieves better results and earns profit while obtaining the label value. These attributes are called more profitable attributes. When the study was examined, the graphs below were obtained when the model was asked to compare the weights and gains between the features at the end of the training.

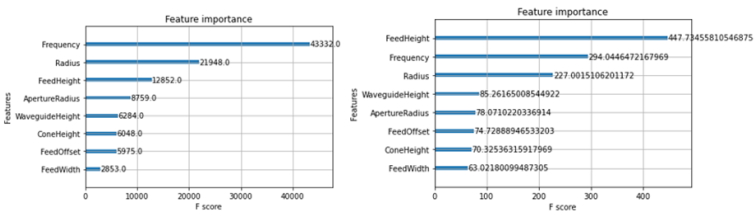

Figure 7: The mod heaviest and most profitable attributes

Conclusions

In this study, when this model, which was trained with the training set and tested with the test set, was examined, three performance metric values and performance rates were obtained. In this study, when this model, which was trained with the training set and tested with the test set, was examined, three performance metric values and performance rates were obtained. These values are respectively: accuracy score for training 96%, MSE value 2.429877, RMSE value 1.558806 and R2 value 0.943632. When these results are examined, it can be seen that the scattering parameter predictions made by the model are close to the real values because the MSE and RMSE values are small and the R2 value is close to 1. This result is also seen in the result graph showing the actual values and the predictions made by the model.

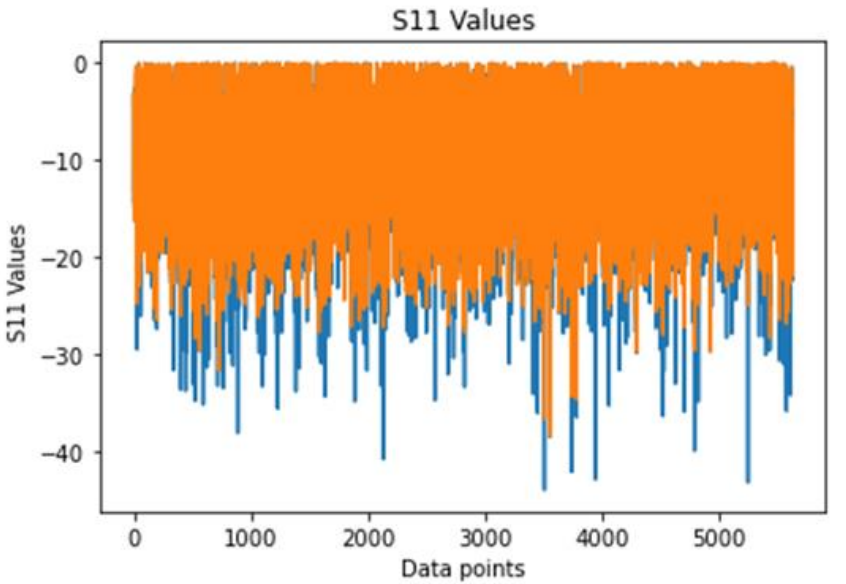

Figure 8: Graph of real and predicted values

Thus, this study demonstrated the advantages of using machine learning algorithms when designing horn antennas, reinforced the importance of using artificial intelligence in the field of communication, and achieved the expected results.

References

Angiulli, G. (2009). Comments on "A Hybrid Method Based on Combining Artificial Neural Network and Fuzzy Inference System for Simultaneous Computation of Resonant Frequencies of Rectangular, Circular, and Triangular Microstrip Antennas. IEEE Transactions on Antennas and Propagation, 57(1), 296–296. https://doi.org/10.1109/TAP.2008.2009786

Bongard, M., Grunert, K., & Aleksic, S. (2020). Techno-Economic Analysis of Deployment Options for Converged 5G Wireless-Optical Access Networks. 2020 43rd International Convention on Information, Communication and Electronic Technology (MIPRO), 401–406. https://doi.org/10.23919/MIPRO48935.2020.9245174

Chen, X., Wang, J., & Chang, L. (2023). Extremely Low-Profile Dual-Band Microstrip Patch Antenna Using Electric Coupling for 5G Mobile Terminal Applications. IEEE Transactions on Antennas and Propagation, 71(2), 1895–1900. https://doi.org/10.1109/TAP.2022.3217640

Coburn, W., & McCormick, S. (2018). Ultra-wideband antenna performance comparison. 2018 International Applied Computational Electromagnetics Society Symposium (ACES), 1–2. https://doi.org/10.23919/ROPACES.2018.8364193

Fang, Y., Tang, M., & Zhang, Y. P. (2022). A Decoupling Structure for Mutual Coupling Suppression in Stacked Microstrip Patch Antenna Array. IEEE Antennas and Wireless Propagation Letters, 21(6), 1110–1114. https://doi.org/10.1109/LAWP.2022.3158420

Jie, G., Jinsong, D., Xing, T., & Rigang, C. (2017). Design of radar antenna based on HFSS. 2017 2nd International Conference on Robotics and Automation Engineering (ICRAE), 460–463. https://doi.org/10.1109/ICRAE.2017.8291430

Jin, Y., Lee, H., & Choi, J. (2018). A Compact, Wideband, Two-Port Substrate-Integrated Waveguide Antenna With a Central, Double-Slotted, Metallic Plate Flanked by Two Paired of Corrugations for Radar Applications. IEEE Transactions on Antennas and Propagation, 66(11), 6376–6381. https://doi.org/10.1109/TAP.2018.2863263

Khan, I., Tian, Y.-B., Inamullah, Vllah, H., Rahman, S. U., & Kamal, M. M. (2018). Design Annular Ring Microstrip Antenna Based on Artificial Neural Network. 2018 2nd IEEE Advanced Information Management,Communicates,Electronic and Automation Control Conference (IMCEC), 2033–2037. https://doi.org/10.1109/IMCEC.2018.8469582

Khan, T., & De, A. (2012). A generalized neural simulator for computing different parameters of circular/triangular microstrip antennas simultaneously. 2012 IEEE Asia-Pacific Conference on Applied Electromagnetics (APACE), 350–354. https://doi.org/10.1109/APACE.2012.6457692

Lee, N., Im, C., Park, S., & Choo, H. (2023). Design of a Metal 3D Printed Double-Ridged Horn Antenna With Stable Gain and Symmetric Radiation Pattern Over a Wide Frequency Range. IEEE Access, 11, 100565–100572. https://doi.org/10.1109/ACCESS.2023.3313724

Mahouti, P., Belen, M. A., Calik, N., & Koziel, S. (2022). Computationally Efficient Surrogate-Assisted Design of Pyramidal-Shaped 3-D Reflectarray Antennas. IEEE Transactions on Antennas and Propagation, 70(11), 10777–10786. https://doi.org/10.1109/TAP.2022.3191131

Montalvo, J., Arroyo, M., Torrijos, J. A., Lorca, J., & Berberana, I. (2015). Fixed-mobile convergence and virtualization in 5G optical transport networks. 2015 17th International Conference on Transparent Optical Networks (ICTON), 1–4. https://doi.org/10.1109/ICTON.2015.7193560

Ren, Z., Qi, S.-S., Wu, W., & Shen, Z. (2021). Pattern-Reconfigurable Water Horn Antenna. IEEE Transactions on Antennas and Propagation, 69(8), 5084–5089. https://doi.org/10.1109/TAP.2021.3064036

Tirkas, P. A., & Balanis, C. A. (n.d.). Finite-difference time-domain technique for radiation by horn antennas. Antennas and Propagation Society Symposium 1991 Digest, 1750–1753. https://doi.org/10.1109/APS.1991.175196

Trzebiatowski, K., Kalista, W., Rzymowski, M., Kulas, L., & Nyka, K. (2022). Multibeam Antenna for Ka-Band CubeSat Connectivity Using 3-D Printed Lens and Antenna Array. IEEE Antennas and Wireless Propagation Letters, 21(11), 2244–2248. https://doi.org/10.1109/LAWP.2022.3189073

Valagiannopoulos, C. A., & Tsitsas, N. L. (2008). Complex resonant frequencies of multi-layered spherical microstrip antennas. 2008 12th International Conference on Mathematical

Methods in Electromagnetic Theory, 213–215. https://doi.org/10.1109/MMET.2008.4580943

Wu, L., Wang, C., Peng, S., & Guo, Y. (2020). 3-D Printed Wideband Millimeter-Wave Horn Antenna With Conical Radiation Pattern. IEEE Antennas and Wireless Propagation Letters, 19(3), 453–456. https://doi.org/10.1109/LAWP.2019.2963747

Yan, Y.-M., Kong, Y.-D., & Chu, Q.-X. (2021). A Compact and High Gain SIW H-Plane Horn Antenna With Stepped Hard Boundary Condition. 2021 13th International Symposium on Antennas, Propagation and EM Theory (ISAPE), 1–3. https://doi.org/10.1109/ISAPE54070.2021.9753634

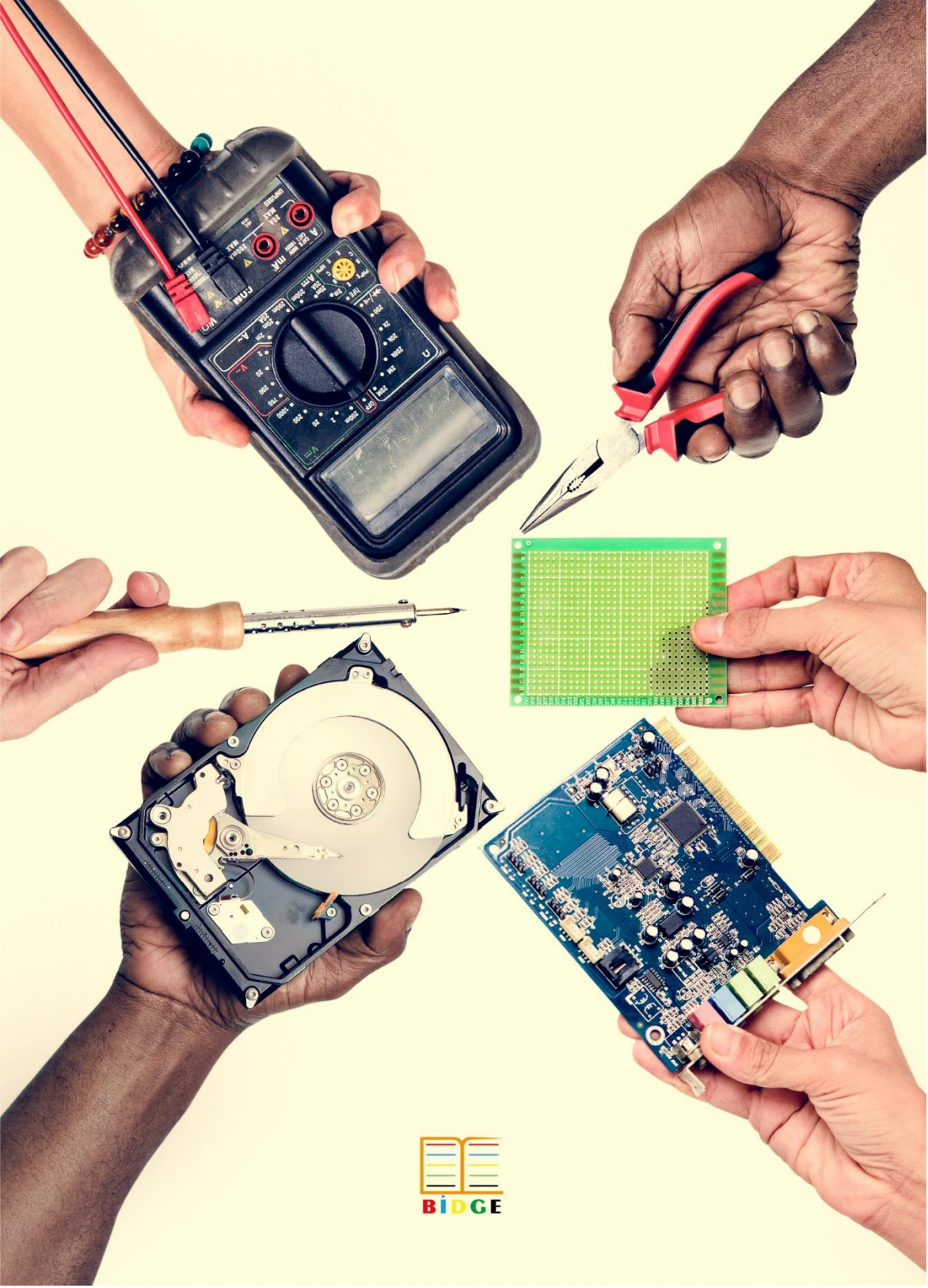
BİDGE